A unified stochastic particle method based on the Bhatnagar-Gross-Krook model for polyatomic gases and its combination with DSMC

Fei Fei [a,b,*], Yuan Hu [c,**], Patrick Jenny [b]

[a] *School of Aerospace Engineering, Huazhong University of science and technology, 430074 Wuhan, China*
[b] *Institute of Fluid Dynamics, ETH Zürich, Sonneggstrasse 3, CH-8092 Zürich, Switzerland*
[c] *State Key Laboratory of High Temperature Gas Dynamics, Institute of Mechanics, Chinese Academy of Sciences, 100190 Beijing, China*

ARTICLE INFO

ABSTRACT

Simulating hypersonic flow around a space vehicle is challenging because of the multi-scale and nonequilibrium nature inherent in these flows. To effectively deal with such flows, a hybrid scheme combining the stochastic particle Bhatnagar-Gross-Krook (BGK) method with direct simulation Monte Carlo (DSMC) was developed recently, but only for monatomic gases (Fei et al. (2021) [29]). In this paper, the particle-particle hybrid method is extended to polyatomic gas flows. In the near continuum regime, employing the Ellipsoidal–Statistical BGK model proposed by Dauvois et al. (2021) [22] with discrete levels of vibrational energy, the stochastic particle BGK method for polyatomic gases is first established following the idea of the unified stochastic particle BGK (USP-BGK) scheme. It is proven to be of second-order accuracy in the fluid limit. After that, the USP-BGK scheme with rotational and vibrational energies is combined with DSMC to construct a hybrid scheme. The present hybrid scheme for polyatomic gases is validated with numerical tests of homogeneous relaxation, 1D shock structure and 2D hypersonic flows past a wedge and a cylinder. Compared to the other stochastic particle methods, the proposed hybrid scheme can achieve higher accuracy at a much lower computational cost. Therefore, it is a more efficient tool to study multiscale hypersonic flows.

© 2022 Elsevier Inc. All rights reserved.

1. Introduction

Hypersonic gas flows about re-entry space vehicles always exhibit multiscale and nonequilibrium phenomena [1]. For the vibrational thermal nonequilibrium, we can still use traditional computational fluid dynamics (CFD) methods most of the time, if vibrational modes are modeled by an additional energy equation [2]. However, for the translational and rotational thermal nonequilibrium, the continuum equations break down as the Knudsen (Kn) number increases. In this rarefied regime, instead of the continuum equations, the Boltzmann equation is required to describe the details of molecular motions and collisions. Due to the complexity and high dimensionality of the collision operator, numerically solving the Boltzmann equation is not easy. One of the popular Boltzmann solvers for hypersonic flows is direct simulation Monte Carlo (DSMC) proposed by Bird [3]. Using stochastic particles, the DSMC method can dramatically reduce the difficulty of

---

* Corresponding author at: School of Aerospace Engineering, Huazhong University of science and technology, 430074 Wuhan, China.
** Corresponding author.
E-mail addresses: ffei@hust.edu.cn (F. Fei), yhu@imech.ac.cn (Y. Hu).

high dimensionality. But its efficiency in the continuum regime is quite low as the time step and cell size restrictions are dictated by the mean collision time and mean free path, respectively. Therefore, simulating multiscale flows with DSMC alone is computationally very expensive.

These time step and cell size restrictions of DSMC (as discussed in [3]) are caused by two issues: the stiffness of the Boltzmann collision term [4] and the decoupling of molecular motion and collision in the implementations [5]. For the first problem, certain modifications already exist which improve the collision calculation for near continuum flows [4,6,7]. Conversely, from the viewpoint of the kinetic model, one also can circumvent the complexity of the Boltzmann collision term using simplified kinetic models, such as the Bhatnagar–Gross–Krook (BGK) [8] model or Fokker-Planck (FP) model [9]. The BGK model was first proposed to model monoatomic gas flow and then was extended for applications that include rotational and vibrational energies [12–17]. As the original BGK model assumes a constant Prandtl number equal to one, two kinds of modified BGK models were introduced to ensure correct transport properties, such as the Ellipsoidal–Statistical BGK model (ES-BGK) [18] and the Shakhov BGK model [19]. Correspondingly, the BGK models for polyatomic gases can also be categorized into these two types [20,21]. Superior to the Shakhov model, according to our knowledge, only the ES-BGK model was proven to satisfy the H-theorem in kinetic theory [21]. Recently, an ES-BGK model with discrete levels of vibrational energy was proposed by Dauvois et al. [22], which satisfies the H-theorem and corrects the Prandtl number. Most of the BGK models were constructed by assuming a continuous distribution of vibrational energy. However, with discrete vibrational energy, Dauvois' ES-BGK model can better approach the physics of hypersonic flows. Therefore, it is selected in the present work. In addition, it is worthwhile to mention that the FP model has also been extended for polyatomic gases by Gorji and Jenny [23] and by Mathiaud and Mieussens [24,25].

It is noted that these simplified kinetic models can lead to very efficient stochastic particle methods [10,11]. However, if a stochastic particle method was implemented in a similar way as conventional DSMC, i.e., by simply splitting molecular motions and collisions, its accuracy would reduce to first order in the fluid limit [5,26]. To avoid this strong numerical dissipation, Jenny et al. proposed a time integration scheme to solve the molecular motions and collisions simultaneously in the Fokker-Planck method [9]. Otherwise, the time step and cell size in stochastic particle methods should be severely restricted like DSMC. Recently, a modified stochastic particle method named the unified stochastic particle BGK method (USP-BGK) was developed [26] for monatomic gases. In the USP-BGK method, the collision term was decomposed into continuous and rarefied parts. Then, by resolving the continuous part with a high-order scheme, the USP-BGK method can achieve second-order accuracy in the fluid limit.

Another problem with BGK and FP stochastic particle methods is that both BGK and FP models only are applicable when the Knudsen number is not too large [27]. For multiscale flows with a wide range of the Knudsen number, a simple choice is to combine a stochastic particle method of the BGK or FP type with DSMC. Different hybrid methods already exist, in which DSMC is coupled with BGK [28,29] or FP [30–33] solvers. Compared to the CFD-DSMC hybrid schemes [34–36], particle-particle hybrid methods are free of the strict requirements on positioning the hybrid interface and no instabilities occur due to the coupling of deterministic and stochastic algorithms [37].

For the purpose of efficiently simulating multiscale hypersonic gas flows, in this paper, a USP-BGK method for polyatomic gases is first developed to improve the accuracy of the traditional stochastic particle methods in the fluid limit, and then the proposed USP-BGK method is combined with DSMC to develop an efficient and robust hybrid scheme for applications over the whole range of the Knudsen number. Our paper is organized as follows: in section 2, the ES-BGK model for polyatomic gases in Ref. [22] is reviewed. Based on this ES-BGK model, a traditional stochastic particle method is introduced in section 3. After that, the USP-BGK method for polyatomic gases is proposed and analyzed in section 4. Further, a corresponding hybrid scheme in combination with DSMC is presented in section 5. At last, section 6 provides numerical validations for several typical multiscale gas flows.

2. Review of the ES-BGK model for polyatomic gases

The Bhatnagar-Gross-Krook (BGK) model simplifies the Boltzmann collision term using a relaxation process. Recently, Dauvois et al. [22] proposed an ES-BGK model with discrete levels of vibrational energy for polyatomic gases, which is given by

$$\frac{\partial \mathcal{F}}{\partial t} + V_i \frac{\partial \mathcal{F}}{\partial x_i} = Q(\mathcal{F}) = \frac{1}{\tau_{BGK}}(\mathcal{F}_G - \mathcal{F}), \tag{2.1}$$

where $Q(\mathcal{F})$ denotes the ES-BGK collision term and $\mathcal{F}(\mathbf{V}, I_r, I_v; \mathbf{x}, t) = \rho(\mathbf{x}, t)f(\mathbf{V}, I_r, I_v; \mathbf{x}, t)$ is the mass density function depending on time t and position $\mathbf{x}$. Further, ρ is the gas density and f is the joint probability density function (PDF) of the molecular velocity $\mathbf{V}$, rotational energy I_r and vibrational energy I_v. τ_{BGK} denotes the relaxation time of the ES-BGK model. Since a single relaxation time is not enough to account for the correct Prandtl number as well as the relaxation rate of different internal energies, in the ES-BGK model proposed in Ref. [22] a Gaussian distribution $\mathcal{F}_G$ was introduced to replace the Maxwellian distribution, i.e.,

$$\mathcal{F}_G(\mathbf{V}, I_r, I_v) = \rho g_{tr}(\mathbf{V}) g_{rot}(I_r) g_{vib}(I_v) \tag{2.2}$$

with

$$g_{tr}(\mathbf{V}) = \frac{1}{\sqrt{\det(2\pi\,\Pi)}} \exp\left(-\frac{1}{2}\mathbf{C}^T\Pi^{-1}\mathbf{C}\right), \tag{2.3a}$$

$$g_{rot}(I_r) = \frac{\Lambda(\delta_{rot})}{(RT_{rot}^{rel})^{\delta_{rot}/2}} I_r^{\frac{\delta_{rot}-2}{2}} \exp\left(-\frac{I_r}{RT_{rot}^{rel}}\right) \quad \text{and} \tag{2.3b}$$

$$g_{vib}(I_v) = \left[1 - \exp\left(-\frac{T_0}{T_{vib}^{rel}}\right)\right] \exp\left(-\frac{I_v}{RT_{vib}^{rel}}\right), \tag{2.3c}$$

where $\mathbf{C} = \mathbf{V} - \mathbf{U}$ is the peculiar molecular velocity and $\mathbf{U}$ is the mean velocity. $g_{tr}(\mathbf{V})$, $g_{rot}(I_r)$ and $g_{vib}(I_v)$ are distribution functions associated with the translational, rotational and vibrational energies of the gaseous molecules. $\Lambda(\delta) = 1/\Gamma(\delta/2)$ and Γ is the usual gamma function. For clarity, the functions $E_i(\mathcal{F}) = e_i(T_i)$ that map translational, rotational and vibrational temperature to the corresponding energies are defined as [22]

$$E_{tr}(\mathcal{F}) = e_{tr}(T_{tr}) = \frac{3}{2}RT_{tr}, \tag{2.4a}$$

$$E_{rot}(\mathcal{F}) = e_{rot}(T_{rot}) = \frac{\delta_{rot}}{2}RT_{rot} \quad \text{and} \tag{2.4b}$$

$$E_{vib}(\mathcal{F}) = e_{vib}(T_{vib}) = \frac{RT_0}{\exp(T_0/T_{vib}) - 1}, \tag{2.4c}$$

where δ_{rot} is the number of degrees of freedom of rotation, and T_0 is the characteristic vibrational temperature. Moreover, the intermediate translational-rotational temperature $T_{tr,rot}$ and equilibrium temperature T_{eq} are defined as

$$e_{tr,rot}(T_{tr,rot}) = E_{tr}(\mathcal{F}) + E_{rot}(\mathcal{F}) \quad \text{and} \tag{2.5a}$$

$$e(T_{eq}) = E_{tr}(\mathcal{F}) + E_{rot}(\mathcal{F}) + E_{vib}(\mathcal{F}). \tag{2.5b}$$

According to Eqs. (2.4) and (2.5), related temperatures can be obtained from the inverse functions

$$T_{tr} = e_{tr}^{-1}(E_{tr}), \qquad T_{rot} = e_{rot}^{-1}(E_{rot}) \quad \text{and} \quad T_{vib} = e_{vib}^{-1}(E_{vib}), \tag{2.6}$$

and

$$T_{tr,rot} = e_{tr,rot}^{-1}(E_{tr} + E_{rot}) \quad \text{and} \quad T_{eq} = e^{-1}(E_{tr} + E_{rot} + E_{vib}). \tag{2.7}$$

The translational, rotational and vibrational energies of the gas can be obtained from the ensemble average as

$$\rho E_{tr}(\mathcal{F}) = \left\langle \frac{1}{2}C^2\mathcal{F} \right\rangle_{V,I_r,I_v}, \qquad \rho E_{rot}(\mathcal{F}) = \langle I_r\mathcal{F}\rangle_{V,I_r,I_v} \quad \text{and} \quad \rho E_{vib}(\mathcal{F}) = \langle I_v\mathcal{F}\rangle_{V,I_r,I_v}. \tag{2.8}$$

For the discrete vibrational modes $I_v = iRT_0$ and $\langle\phi\rangle_{V,I_r,i} = \sum_{i=0}^{+\infty}\int_{\mathbb{R}^3}\int_{\mathbb{R}}\phi(\mathbf{V},I_r,i)dI_rd\mathbf{V}$ denotes the integral of any function ϕ.

In the Gaussian distribution (2.2) the covariance matrix Π, the temperatures T_{rot}^{rel} and T_{vib}^{rel} are employed to fit different relaxation times and given by Ref. [22], i.e.,

$$\Pi = \eta RT_{eq}\mathbf{I} + (1-\eta)\left[\theta RT_{tr,rot}\mathbf{I} + (1-\theta)(\nu\Theta + (1-\nu)RT_{tr}\mathbf{I})\right], \tag{2.9}$$

$$e_{rot}^{rel} = \eta e_{rot}(T_{eq}) + (1-\eta)\left[\theta e_{rot}(T_{tr,rot}) + (1-\theta)E_{rot}(\mathcal{F})\right], \tag{2.10}$$

$$e_{vib}^{rel} = \eta e_{vib}(T_{eq}) + (1-\eta)E_{vib}(\mathcal{F}), \tag{2.11}$$

where η, θ and ν are relaxation coefficients. Θ is related to a pressure tensor, i.e.,

$$\rho\Theta = \langle\mathbf{C}\otimes\mathbf{C}\mathcal{F}\rangle_{V,I_r,I_v}, \tag{2.12}$$

and T_{rot}^{rel} and T_{vib}^{rel} are calculated from e_{rot}^{rel} and e_{vib}^{rel} as

$$T_{rot}^{rel} = e_{rot}^{-1}\left(e_{rot}^{rel}\right) \quad \text{and} \quad T_{vib}^{rel} = e_{vib}^{-1}\left(e_{vib}^{rel}\right). \tag{2.13}$$

The transfer between translational and rotational energies and that between translational-rotational and vibrational energies is determined by the relaxation coefficients θ and η, respectively. As shown in Ref. [22],

$$\eta = \frac{1}{Z_{vib}} \quad \text{and} \quad \theta = \frac{1/Z_{rot} - 1/Z_{vib}}{1 - 1/Z_{vib}}, \tag{2.14}$$

where Z_{rot} and Z_{vib} are the collision numbers describing the relaxation rate of the rotational and vibrational energies to equilibrium. Assuming τ_{rot} and τ_{vib} as their relaxation times, one obtains

$$\tau_{rot} = \tau_{BGK} Z_{rot} \quad \text{and} \quad \tau_{vib} = \tau_{BGK} Z_{vib}. \tag{2.15}$$

The relaxation coefficient ν is used to correct the Prandtl number of the ES-BGK model, i.e.,

$$\text{Pr} = \frac{1}{1 - (1 - \eta)(1 - \theta)\nu}. \tag{2.16}$$

Finally, Dauvois et al. [22] obtain the relaxation time of the ES-BGK model as

$$\tau_{BGK} = \frac{\mu}{p} [1 - (1 - \eta)(1 - \theta)\nu], \tag{2.17}$$

where μ and p are gas viscosity and pressure, respectively.

3. Traditional stochastic particle method based on the ES-BGK model

To solve the kinetic equation (2.1) numerically, a stochastic particle method can be employed. Gallis and Torczynski [10] first developed the stochastic particle method based on the ES-BGK model for monoatomic gases, and then it was extended to include internal energies by other authors [38–40]. Generally, this traditional stochastic particle method (SP-BGK) employs a simple time splitting scheme like DSMC. Therefore, its governing equation can be obtained by dividing Eq. (2.1) into a transport step and a collision step, i.e.,

$$\text{transport step}: \quad \frac{\partial \mathcal{F}}{\partial t} + V_i \frac{\partial \mathcal{F}}{\partial x_i} = 0 \quad \text{and} \tag{3.1a}$$

$$\text{collision step}: \quad \frac{\partial \mathcal{F}}{\partial t} = Q(\mathcal{F}). \tag{3.1b}$$

Similar to DSMC, the SP-BGK method solves governing equation (3.1) using randomly sampled computational particles. A review of the traditional SP-BGK algorithm for monoatomic gases can be found in refs. [26,52]. In the following, this algorithm is extended for the polyatomic gas flows.

The transport step is updated by moving the computational particles with their molecular velocities. Thus, the solution of Eq. (3.1a) yields

$$\mathcal{F}^*(\mathbf{V}, I_r, I_v; \mathbf{x}, \Delta t) = \mathcal{F}(\mathbf{V}, I_r, I_v; \mathbf{x} - \mathbf{V}\Delta t, t^n), \tag{3.2}$$

where $\mathcal{F}^*$ is the intermediate distribution function after particle movement.

Then, by setting $\mathcal{F}^*$ as the initial condition, the distribution function after the collision step is calculated as

$$\mathcal{F}(\mathbf{V}, I_r, I_v; \mathbf{x}, t^{n+1}) = \mathcal{F}^*(\mathbf{V}, I_r, I_v; \mathbf{x}, \Delta t)e^{-\Delta t/\tau_{BGK}}$$
$$+ \left(1 - e^{-\Delta t/\tau_{BGK}}\right) \int\limits_0^{\Delta t} \frac{e^{t'/\tau_{BGK}}}{\tau_{BGK}\left(e^{\Delta t/\tau_{BGK}} - 1\right)} \mathcal{F}_G(\mathbf{V}, I_r, I_v; \mathbf{x}, t')dt'. \tag{3.3}$$

If $\mathcal{F}_G(\mathbf{V}, I_r, I_v; \mathbf{x}, t')$ in the second term of the right-hand side of Eq (3.3) is assumed to be constant during the collision step, Eq. (3.3) can be further simplified as

$$\mathcal{F}(\mathbf{V}, I_r, I_v; \mathbf{x}, t^{n+1}) = e^{-\Delta t/\tau_{BGK}} \mathcal{F}^*(\mathbf{V}, I_r, I_v; \mathbf{x}, \Delta t) + \left(1 - e^{-\Delta t/\tau_{BGK}}\right) \mathcal{F}_G^*(\mathbf{V}, I_r, I_v; \mathbf{x}, \Delta t). \tag{3.4}$$

Eq. (3.4) is usually solved by randomly separating the computational particles into two sets [10,38–40]: the first set with $e^{-\Delta t/\tau_{BGK}} N_c$ and the second set with $\left(1 - e^{-\Delta t/\tau_{BGK}}\right) N_c$ particles. N_c is the particle number in the calculated cell. Particle velocity, rotational and vibrational energies of the first set remain unchanged, while those of the second set are updated according to $\mathcal{F}_G^*(\mathbf{V}, I_r, I_v; \mathbf{x}, \Delta t)$. A Metropolis-Hastings (MH) method [52] can be employed to sample the velocities, rotational and vibrational energies from this Gaussian distribution $\mathcal{F}_G^*(\mathbf{V}, I_r, I_v; \mathbf{x}, \Delta t)$ (the details of the MH algorithm are given in Appendix A).

Generally, the Gaussian distribution $\mathcal{F}_G(\mathbf{V}, I_r, I_v; \mathbf{x}, t')$, which depends on $\mathbf{\Pi}(t')$, $E_{tr}(t')$, $E_{rot}(t')$ and $E_{vib}(t')$, is not constant during the collision process. Therefore, the accurate solution of Eq. (3.3) should be evaluated. According to the second term on the right-hand side of Eq. (3.3), the second set of $\left(1 - e^{-\Delta t/\tau_{BGK}}\right) N_c$ particles need to be resampled from the distribution $\mathcal{F}_G(\mathbf{V}, I_r, I_v; \mathbf{x}, t')$ instead. For this purpose, a Monte Carlo algorithm has been proposed in Ref. [26] for monoatomic gases. The present work extends this algorithm to polyatomic gases. First, a certain time t' in the range $[0, \Delta t]$ is sampled as

$$t' = \tau_{BGK} \ln\left[rand \cdot \left(e^{\Delta t/\tau_{BGK}} - 1\right) + 1\right] \tag{3.5}$$

using Monte Carlo, where $rand$ is a random number between 0 and 1. After the certain time t' is known, $\mathcal{F}_G(\mathbf{V}, I_r, I_v; \mathbf{x}, t')$ can be estimated from the values of $\mathbf{\Pi}(t')$, $E_{tr}(t')$, $E_{rot}(t')$ and $E_{vib}(t')$ and sampled by the MH method again. In addition, the solution of $\mathbf{\Pi}(t')$, $E_{tr}(t')$, $E_{rot}(t')$ and $E_{vib}(t')$ are calculated using the moment equations of Eq. (2.1) (see Appendix B).

4. The USP-BGK method for polyatomic gases

By introducing characteristic variables, such as x_*, ρ_*, T_* and $V_* = \sqrt{RT_*}$, $I_{r*} = RT_*$ and $I_{v*} = RT_*$, the ES-BGK collision term as shown in Eq. (2.1) can be rewritten in a dimensionless form, i.e.,

$$Q(\mathcal{F}) = \frac{1}{\varepsilon}(\mathcal{F}_G - \mathcal{F}), \tag{4.1}$$

where $\varepsilon = \tau_{BGK} V_* / x_*$ denotes the Knudsen number. For simplicity, all the equations below, unless specified, will be presented in dimensionless forms. It is noted that the BGK equation also shows strong stiffness in the continuum regime. Since the traditional SP-BGK method employs the simple splitting scheme, this stiffness of the BGK collision term will reduce its order of accuracy in the fluid limit [5]. It has been proved that traditional SP-BGK methods turn to first order in the fluid limit and suffer from low accuracy and efficiency [26]. To overcome this defect, a unified stochastic particle BGK method (USP-BGK) for polyatomic gases is developed in the present work. To summarize, the proposed scheme possesses the following features:

- The scheme is capable of simulating polyatomic gas flows in the whole range of the Knudsen number;
- The scheme is second-order accurate in the fluid limit;
- The scheme is asymptotic-preserving (AP) of the Navier-Stokes equations.

Remark 4.1. From the viewpoint of the numerical scheme, assuming the time step size Δt is fixed, we refer to the fluid limit as $\varepsilon \to 0$, and the kinetic limit as $\varepsilon \to +\infty$. However, the definitions of the continuum and rarefied regimes are based on the physics and independent of the time step size, i.e., one refers to the continuum regime if $\varepsilon \ll 1$ and to the rarefied regime if $\varepsilon \gg 1$.

4.1. Governing equations and numerical scheme

The main idea of the USP-BGK method [26] is to decompose the collision term of the kinetic model into a continuous part Q_C and a rarefied part $Q_R = Q - Q_C$; then the former one is solved with a high order scheme like the Crank-Nicolson scheme [26] or the DIRK (Diagonally Implicit Runge–Kutta) scheme [53] in the transport step, and the latter one is solved with a time integration scheme like the traditional SP-BGK method in the collision step to achieve the asymptotic-preserving property. Therefore, the governing equations for the unified stochastic particle BGK method are written as

$$\textbf{transport step:} \quad \frac{\partial \mathcal{F}}{\partial t} + V_i \frac{\partial \mathcal{F}}{\partial x_i} = Q_C \quad \text{and} \tag{4.2a}$$

$$\textbf{collision step:} \quad \frac{\partial \mathcal{F}}{\partial t} = Q_R. \tag{4.2b}$$

4.1.1. Construction of Q_C

The continuous part of the collision term is modeled by the Grad expansion, which is constructed by an expansion of Maxwellian with Hermite polynomials [54]. Since the ES-BGK model considers the translational, rotational and vibrational energies individually, similarly a multi-temperature Maxwellian distribution $\mathcal{F}_M$ is assumed to approach the equilibrium state, i.e.,

$$\mathcal{F}_M(\mathbf{V}, I_r, I_v) = \rho M_{tr}(\mathbf{V}) M_{rot}(I_r) M_{vib}(I_v) \tag{4.3}$$

with

$$M_{tr}(\mathbf{V}) = \frac{1}{(2\pi T_{tr})^{3/2}} \exp\left(-\frac{C^2}{2T_{tr}}\right), \tag{4.4a}$$

$$M_{rot}(I_r) = \frac{\Lambda(\delta_{rot})}{(T_{rot})^{\delta_{rot}/2}} I_r^{\frac{\delta_{rot}-2}{2}} \exp\left(-\frac{I_r}{T_{rot}}\right) \quad \text{and} \tag{4.4b}$$

$$M_{vib}(I_v) = \left[1 - \exp\left(-\frac{T_0}{T_{vib}}\right)\right] \exp\left(-\frac{I_v}{T_{vib}}\right). \tag{4.4c}$$

Then based on this equilibrium distribution, we can construct Q_C as a Grad distribution using the first nine moments, i.e.,

$$Q_C = \mathcal{F}_{|Grad}(\mathbf{V}, I_r, I_v; \rho, \rho\mathbf{U}, \rho E_{tr}, \rho E_{rot}, \rho E_{vib}, \boldsymbol{\sigma}, \mathbf{q}_{tr}, \mathbf{q}_{rot}, \mathbf{q}_{vib}), \tag{4.5}$$

where $\boldsymbol{\sigma} = \langle(\mathbf{C} \otimes \mathbf{C} - T_{tr}\mathbf{I})\mathcal{F}\rangle_{V,I_r,I_v}$ is the shear stress. $\mathbf{q}_{tr} = \langle\mathbf{C}C^2/2\mathcal{F}\rangle_{V,I_r,I_v}$, $\mathbf{q}_{rot} = \langle\mathbf{C}I_r\mathcal{F}\rangle_{V,I_r,I_v}$ and $\mathbf{q}_{vib} = \langle\mathbf{C}I_v\mathcal{F}\rangle_{V,I_r,I_v}$ are heat fluxes due to translational, rotational and vibrational energies, respectively. The expansion coefficients of the Grad

distribution are calculated to ensure that these low order moments of the continuous part are equal to those of the original collision term, i.e.,

$$\langle \phi Q_C \rangle_{V, I_r, I_v} = \langle \phi Q (\mathcal{F}) \rangle_{V, I_r, I_v}. \tag{4.6}$$

Corresponding to the first nine moments, $\phi = \left(1, \mathbf{V}, \frac{1}{2}C^2, I_r, I_v, \mathbf{C} \otimes \mathbf{C} - T_{tr}\mathbf{I}, \frac{1}{2}\mathbf{C}C^2, \mathbf{C}I_r, \mathbf{C}I_v\right)^T$ is a vector of polynomials of the molecular velocity, rotational and vibrational energies. After straightforward computation, Q_C is obtained as

$$
Q_C = -\frac{1}{\varepsilon}\mathcal{F}_M \left\{
\begin{array}{l}
\dfrac{1}{2p\,\mathrm{Pr}}\left[\dfrac{\mathbf{C}\otimes\mathbf{C}}{T_{tr}} - \dfrac{1}{3}\dfrac{C^2}{T_{tr}}\mathbf{I}\right] : \boldsymbol{\sigma} \\[3mm]
+\dfrac{2}{5T_{tr}p}\left(\dfrac{C^2}{2T_{tr}} - \dfrac{5}{2}\right)\mathbf{C}\cdot\mathbf{q}_{tr} + \dfrac{2}{\delta_{rot}T_{rot}p}\left(\dfrac{I_r}{T_{rot}} - \dfrac{\delta_{rot}}{2}\right)\mathbf{C}\cdot\mathbf{q}_{rot} \\[3mm]
+\dfrac{1}{T_{vib}\frac{\partial e_{vib}}{\partial T_{vib}}p}\left(\dfrac{I_v}{T_{vib}} - \dfrac{\delta_{vib}(T_{vib})}{2}\right)\mathbf{C}\cdot\mathbf{q}_{vib} \\[3mm]
-\dfrac{1}{T_{tr}}\left(\dfrac{C^2}{2T_{tr}} - \dfrac{3}{2}\right)\left[\eta\left(T_{eq} - T_{tr}\right) + (1-\eta)\left(\dfrac{3\theta}{3+\delta_{rot}}E_{rot} - \dfrac{\theta\delta_{rot}}{3+\delta_{rot}}E_{tr}\right)\Big/\left(\dfrac{3}{2}\right)\right] \\[3mm]
-\dfrac{1}{T_{rot}}\left(\dfrac{I_r}{T_{rot}} - \dfrac{\delta_{rot}}{2}\right)\left[\eta\left(T_{eq} - T_{rot}\right) + (1-\eta)\left(-\dfrac{3\theta}{3+\delta_{rot}}E_{rot} + \dfrac{\theta\delta_{rot}}{3+\delta_{rot}}E_{tr}\right)\Big/\left(\dfrac{\delta_{rot}}{2}\right)\right] \\[3mm]
-\dfrac{\eta}{T_{vib}}\left(\dfrac{I_v}{T_{vib}} - \dfrac{\delta_{vib}(T_{vib})}{2}\right)\left[e_{vib}(T_{eq}) - E_{vib}\right]\Big/\left(\dfrac{\partial e_{vib}}{\partial T_{vib}}\right)
\end{array}
\right\}, \tag{4.7}
$$

where $\dfrac{\partial e_{vib}(T_{vib})}{\partial T_{vib}} = \dfrac{T_0^2}{T_{vib}^2}\left\{\exp\left(\dfrac{T_0}{T_{vib}}\right)\Big/\left[\exp\left(\dfrac{T_0}{T_{vib}}\right) - 1\right]^2\right\}$, $\delta_{vib}(T_{vib}) = \dfrac{2T_0/T_{vib}}{\exp(T_0/T_{vib}) - 1}$ denotes the number of vibrational degrees of freedom and $p = \rho T_{tr}$ is the pressure.

4.1.2. Numerical scheme

In the USP-BGK method, the transport and collision steps are implemented in a sequence. They are numerically solved as follows:

For the transport step, the Crank-Nicolson scheme is applied for Eq. (4.2a), and the numerical solution along characteristics is given by

$$
\begin{aligned}
\mathcal{F}^*(\mathbf{V}, I_r, I_v; \mathbf{x}, \Delta t) = \frac{\Delta t}{2}&\left[Q_C^*(\mathbf{V}, I_r, I_v; \mathbf{x}, \Delta t) + Q_C(\mathbf{V}, I_r, I_v; \mathbf{x} - \mathbf{V}\Delta t, t^n)\right] \\
&+ \mathcal{F}(\mathbf{V}, I_r, I_v; \mathbf{x} - \mathbf{V}\Delta t, t^n)
\end{aligned} \tag{4.8}
$$

For the collision step, taking the intermediate PDF $\mathcal{F}^*(\mathbf{V}, I_r, I_v; \mathbf{x}, \Delta t)$ as the initial value and calculating the integration solution of Eq. (4.2b), the final PDF solution is obtained as

$$
\begin{aligned}
\mathcal{F}(\mathbf{V}, I_r, I_v; \mathbf{x}, t^{n+1}) =\ &\mathcal{F}^*(\mathbf{V}, I_r, I_v; \mathbf{x}, \Delta t)e^{-\Delta t/\varepsilon} \\
&+ \left(1 - e^{-\Delta t/\varepsilon}\right)\mathcal{F}_G^*(\mathbf{V}, I_r, I_v; \mathbf{x}, \Delta t) - \varepsilon\left(1 - e^{-\Delta t/\varepsilon}\right)\cdot Q_C^*(\mathbf{V}, I_r, I_v; \mathbf{x}, \Delta t)
\end{aligned} \tag{4.9}
$$

Different from the solution of the SP-BGK method as shown in Eq. (3.3), since $\langle \phi Q_C \rangle_{V, I_r, I_v} = \langle \phi Q (\mathcal{F}) \rangle_{V, I_r, I_v}$ for the low order moments, the USP-BGK method yields $\mathcal{F}_G(\mathbf{V}, I_r, I_v; \mathbf{x}, t') = \mathcal{F}_G^*(\mathbf{V}, I_r, I_v; \mathbf{x}, \Delta t)$ in the time integration $t' \in [0, \Delta t]$.

4.1.3. The asymptotic property

For the fluid limit, as $\Delta t/\varepsilon \gg 1$, the integration solution of the collision step (Eq. (4.9)) approaches

$$\mathcal{F}(\mathbf{V}, I_r, I_v; \mathbf{x}, t^{n+1}) = \mathcal{F}_G^*(\mathbf{V}, I_r, I_v; \mathbf{x}, \Delta t) - \varepsilon Q_C^*(\mathbf{V}, I_r, I_v; \mathbf{x}, \Delta t). \tag{4.10}$$

Using the Chapman-Enskog analysis, we have

$$Q_C^*(\mathbf{V}, I_r, I_v; \mathbf{x}, \Delta t) = \frac{\partial_0 M^*}{\partial t} + \mathbf{V} \cdot \nabla M^* + O(\varepsilon), \tag{4.11}$$

where M is the Maxwellian distribution based on the equilibrium temperature, i.e.,

$$
\begin{aligned}
M(\mathbf{V}, I_r, I_v) =\ &\rho\frac{1}{\left(2\pi T_{eq}\right)^{3/2}}\exp\left(-\frac{(\mathbf{V} - \mathbf{U})^2}{2T_{eq}}\right) \\
&\cdot\frac{\Lambda(\delta_{rot})}{(T_{eq})^{\delta_{rot}/2}}I_r^{\frac{\delta_{rot}-2}{2}}\exp\left(-\frac{I_r}{T_{eq}}\right)\cdot\left[1 - \exp\left(-\frac{T_0}{T_{eq}}\right)\right]\exp\left(-\frac{I_v}{T_{eq}}\right)
\end{aligned} \tag{4.12}
$$

Substituting Eq. (4.11) into Eq. (4.10), one obtains

$$\mathcal{F}(\mathbf{V}, I_r, I_v; \mathbf{x}, t^{n+1}) = \mathcal{F}_G^* - \varepsilon \left(\frac{\partial_0 M^*}{\partial t} + \mathbf{V} \cdot \nabla M^* \right) + O(\varepsilon^2). \tag{4.13}$$

According to Proposition 6.1 of Ref. [22], Eq. (4.13) can be rewritten as

$$\mathcal{F}(\mathbf{V}, I_r, I_v; \mathbf{x}, t^{n+1}) = \mathcal{F}^*(\mathbf{V}, I_r, I_v; \mathbf{x}, \Delta t) + O(\varepsilon^2). \tag{4.14}$$

Substituting the solution of the transport step (4.8) into Eq. (4.14), using $Q_C^*(\mathbf{V}, I_r, I_v; \mathbf{x}, \Delta t) = Q_C(\mathbf{V}, I_r, I_v; \mathbf{x}, t^{n+1})$ and $Q^* = Q_C^* + O(\varepsilon)$ again, we have

$$\mathcal{F}(\mathbf{V}, I_r, I_v; \mathbf{x}, t^{n+1}) = \frac{\Delta t}{2} \left[Q(\mathbf{V}, I_r, I_v; \mathbf{x}, t^{n+1}) + Q(\mathbf{V}, I_r, I_v; \mathbf{x} - \mathbf{V}\Delta t, t^n) \right] \\ + \mathcal{F}(\mathbf{V}, I_r, I_v; \mathbf{x} - \mathbf{V}\Delta t, t^n) + O(\Delta t \varepsilon) \tag{4.15}$$

Expanding the above distribution functions around $\mathbf{x}' = \mathbf{x} - \mathbf{V}\Delta t/2$ and $t' = \Delta t/2$, we can obtain the following equation after some manipulations.

$$\frac{\partial \mathcal{F}}{\partial t} + V_i \frac{\partial \mathcal{F}}{\partial x_i} = Q(\mathcal{F}) + O(\Delta t^2) + O(\varepsilon). \tag{4.16}$$

Its conservation equations are just the Navier-Stokes equations. Obviously, the USP-BGK scheme is asymptotic-preserving of the NS equations. Moreover, from the second term on the right-hand side of Eq. (4.16), we also note that the proposed USP-BGK scheme is of second-order accuracy in the fluid limit.

For the kinetic limit, as $\Delta t/\varepsilon \ll 1$, combining Eqs. (4.8) and (4.9) and using the Taylor expansion, the numerical solution of the USP-BGK method is obtained as

$$\mathcal{F}(\mathbf{V}, I_r, I_v; \mathbf{x}, t^{n+1}) = \mathcal{F}(\mathbf{V}, I_r, I_v; \mathbf{x} - \mathbf{V}\Delta t, t^n)(1 - \Delta t/\varepsilon) \\ + \Delta t/\varepsilon \mathcal{F}_G^*(\mathbf{V}, I_r, I_v; \mathbf{x}, \Delta t) + O(\Delta t/\varepsilon)^2 \tag{4.17}$$

which is consistent with the solution of the traditional SP-BGK method as shown in Eq. (3.4). Therefore, the USP-BGK scheme reduces to the traditional SP-BGK method in the kinetic limit.

4.2. Numerical implementation of the unified stochastic particle method

In the USP-BGK method, the PDF solutions of Eqs. (4.8) and (4.9) are evaluated using stochastic particles. The algorithm of the USP-BGK method can be simplified by introducing the two auxiliary PDFs [29,41]

$$\tilde{\mathcal{F}}^* = \mathcal{F}^* - \frac{\Delta t}{2} Q_C^* \quad \text{and} \tag{4.18a}$$

$$\widehat{\mathcal{F}} = \mathcal{F} + \frac{\Delta t}{2} Q_C. \tag{4.18b}$$

Then, the solution of the transport step (4.8) can be reorganized as

$$\tilde{\mathcal{F}}^*(\mathbf{V}, I_r, I_v; \mathbf{x}, \Delta t) = \widehat{\mathcal{F}}(\mathbf{V}, I_r, I_v; \mathbf{x} - \mathbf{V}\Delta t, t^n). \tag{4.19}$$

Similarly, using $\tilde{\mathcal{F}}^*$ and $\widehat{\mathcal{F}}$, the solution of the collision step (4.9) is rewritten as

$$\widehat{\mathcal{F}}(\mathbf{V}, I_r, I_v; \mathbf{x}, t^{n+1}) = e^{-\Delta t/\varepsilon} \tilde{\mathcal{F}}^*(\mathbf{V}, I_r, I_v; \mathbf{x}, \Delta t) + \left(1 - e^{-\Delta t/\varepsilon} \right) \mathcal{F}_U^*(\mathbf{V}, I_r, I_v; \mathbf{x}, \Delta t), \tag{4.20}$$

where a new target distribution for the unified stochastic particle algorithm is defined as

$$\mathcal{F}_U^*(\mathbf{V}, I_r, I_v; \mathbf{x}, \Delta t) = \mathcal{F}_G^*(\mathbf{V}, I_r, I_v; \mathbf{x}, \Delta t) + \left[\frac{\Delta t}{2} \frac{\left(1 + e^{-\Delta t/\varepsilon} \right)}{\left(1 - e^{-\Delta t/\varepsilon} \right)} - \varepsilon \right] Q_C^*(\mathbf{V}, I_r, I_v; \mathbf{x}, \Delta t). \tag{4.21}$$

By comparing Eqs. (4.19) and (4.20) with Eqs. (3.2) and (3.4), it is noted that the evolution of the original PDF $\mathcal{F}$ in the traditional SP-BGK method is replaced by updating the auxiliary PDF $\widehat{\mathcal{F}}$ in the algorithm of the USP-BGK method. Therefore, USP-BGK, SP-BGK and DSMC can be implemented in a similar way, which is beneficial for the construction of hybrid schemes among these stochastic particle methods.

In detail, the implementations of the USP-BGK method for polyatomic gases are introduced in the following four steps.

Step 1: Initialization

The computational particles are initialized and sampled from the initial distribution $\widehat{\mathcal{F}}(\mathbf{V}, I_r, I_v; \mathbf{x}, 0)$ using the MH algorithm. Their values are $\left\{ \mathbf{X}^{(k)}, \mathbf{M}^{(k)}, I_r^{(k)}, I_v^{(k)} \right\}_{k \in \mathbb{N}}$, where $\mathbf{X}^{(k)}$, $\mathbf{M}^{(k)}$, $I_r^{(k)}$ and $I_v^{(k)}$ denote the position, velocity, rotational and

vibrational energies of the particle k, respectively. Since the initial PDF is mostly assumed to be Maxwellian, thus $Q_C = 0$ and $\widehat{\mathcal{F}}(\mathbf{V}, I_r, I_v; \mathbf{x}, 0) = \mathcal{F}_M(\mathbf{V}, I_r, I_v; \mathbf{x}, 0)$. Therefore the initialization process for the USP-BGK method is the same as that for DSMC.

Step 2: Transport

For the transport step, the velocity, rotational and vibrational energies of the computational particles are unchanged. Their locations, however, are updated along the characteristics, i.e., $\mathbf{X}^{(k)}(t^{n+1}) = \mathbf{X}^{(k)}(t^n) + \mathbf{M}^{(k)}(t^n)\Delta t$ according to Eq. (4.19). In addition, since USP-BGK and DSMC track molecular motions in the same way, the same treatment of the boundary conditions can be applied.

Step 3: Collision

For the collision step, the computational particles are randomly assigned into two sets: the first set with $e^{-\Delta t/\varepsilon} N_c$ and the second set with $\left(1 - e^{-\Delta t/\varepsilon}\right) N_c$. Molecular variables of the first set are unchanged, while those of the second set are updated according to $\mathcal{F}_U^*(\mathbf{V}, I_r, I_v; \mathbf{x}, \Delta t)$. In addition, the macro variables used in the construction of $\mathcal{F}_U^*(\mathbf{V}, I_r, I_v; \mathbf{x}, \Delta t)$ are calculated based on the PDF $\tilde{\mathcal{F}}^*(\mathbf{V}, I_r, I_v; \mathbf{x}, \Delta t)$ after the transport step (see Appendix C).

Step 4: Sampling

At the end of every time step, the macroscopic quantities are sampled from the auxiliary PDFs (see Appendix C) for the USP-BGK method.

4.3. Spatial interpolation

As shown in section 4.1.3, in the fluid limit the USP-BGK method is of second-order accuracy in time. To also achieve the same accuracy in space, a second-order spatial interpolation should be employed [53]. However, directly applying the cell-based interpolation algorithm used in CFD is usually inefficient for a stochastic particle method [42]. First, most of the time, the flow fields sampled from the computational particles suffer from statistical noise, which may influence the accuracy and stability of the cell-based interpolation algorithm. Second, stochastic particle methods perform the computing processes in the local cell, so a CFD cell-based interpolation will bring extra complexity to the simulation code.

Alternatively, a spatial interpolation based on the computational particles was proposed in Ref. [41]. Specifically, in order to calculate the macro quantity $\Phi^{(k)}(\mathbf{x}, t)$ of the kth particle at location $\mathbf{x}$ and time t, this interpolation algorithm is implemented as follows:

(a) A random deviation Δx is first sampled based on symmetric kernel function, e.g., a uniform hat kernel

$$K_{Uniform}(\Delta x) = \begin{cases} 1 & \Delta x \in [-\Delta h/2, \Delta h/2] \\ 0 & otherwise \end{cases}, \tag{4.22}$$

where $\mathbf{\Delta}x = \Delta h \cdot (rand - 0.5)$ is calculated, and *rand* is a uniform random number in $[0, 1]$.

(b) If the sampled new position is located in cell j, i.e., if $\mathbf{x} + \mathbf{\Delta x} \in \Omega_j$, then the interpolated value of the particle k is set to

$$\Phi^{(k)}(\mathbf{x}, t) \equiv \Phi_c(\mathbf{x}_j, t; \mathbf{x} + \mathbf{\Delta x} \in \Omega_j), \tag{4.23}$$

where $\Phi_c(\mathbf{x}_j, t)$ denotes the mean value in cell j.

Since this interpolation algorithm is not dependent on the type of grids, the proposed USP-BGK method can be easily implemented in both unstructured (see numerical case 6.3) and structured (see numerical case 6.4) meshes.

4.4. Conservation of the USP-BGK method

As well known, the stochastic particle BGK method can only ensure the conservation laws in a statistical sense. Therefore, energy and momentum conservation correction steps are performed at the end of the collision step. In theory, according to Eqs. (C.10)–(C.12), accurate translational ($\widehat{E}_{tr}$), rotational ($\widehat{E}_{rot}$) and vibrational ($\widehat{E}_{vib}$) energies based on $\widehat{\mathcal{F}}(\mathbf{V}, I_r, I_v; \mathbf{x}, t^{n+1})$ are determined by the variables before the collision step. However, in practice, due to the nature of the random process, these energies are not exactly conserved. To make them conservative, a correction step for the individual particle (similar to that in Ref. [40]) is implemented as follows.

For the vibrational energy, a modification factor $\alpha_{vib} = \widehat{E}_{vib}/\widehat{E'}_{vib}$ is first calculated, where $\widehat{E'}_{vib}$ denotes the vibrational energy directly averaged from the computational particles after the collision step. Then the vibrational energy level is corrected as

$$i^{(k)} = \text{int}\left(\alpha_{vib} i^{(k)'} + rand\right), \tag{4.24}$$

where $i^{(k)}$ and $i^{(k)'}$ are the vibrational energy levels of the kth particle after and before modification, the operator int denotes the integer part.

Assuming the sum of the translational and vibrational energies are conserved, the modification factor for the translational energy can be calculated as

$$\alpha_{tr} = \sqrt{\left(\widehat{E}_{tr} + \widehat{E}_{vib} - \sum_{k=1}^{N} i^{(k)} R T_0 / N \right) / \widehat{E}'_{tr}}. \tag{4.25}$$

Similarly, $\widehat{E}'_{tr}$ denotes the translational energy averaged from the computational particles before correction. Then the particle velocity is finally modified as

$$\mathbf{M}^{(k)} = \alpha_{tr} \left(\mathbf{M}^{(k)'} - \sum_{k=1}^{N} \mathbf{M}^{(k)'} / N \right) + \mathbf{U}^*, \tag{4.26}$$

where $\mathbf{U}^*$ is the mean velocity before the collision step, which is constant during the collision step. $\mathbf{M}^{(k)}$ and $\mathbf{M}^{(k)'}$ are the velocities of the kth particle after and before the correction, respectively. The conservation of momentum is also ensured by Eq. (4.26).

In addition, the particle's rotational energy is modified as

$$I_r^{(k)} = \alpha_{rot} I_r^{(k)'}, \quad \text{and} \quad \alpha_{rot} = \widehat{E}_{rot} / \widehat{E}'_{rot}, \tag{4.27}$$

where $\widehat{E}'_{rot}$ denotes the rotational energy directly averaged from the computational particles before correction. $I_r^{(k)}$ and $I_r^{(k)'}$ are the rotational energies of the kth particle after and before modification, respectively.

5. The hybrid USPBGK-DSMC method for polyatomic gases

5.1. The hybrid algorithm

USP-BGK is a very efficient and accurate method for flows up to only moderate Knudsen numbers, while DSMC is physically valid for all flow regimes but inefficient for small Knudsen numbers. Consequently, it is desirable to have the hybrid scheme combining USP-BGK and DSMC for the multiscale flows where the Knudsen number varies many orders of magnitude.

The hybrid USPBGK-DSMC method for monatomic gases was proposed recently [29]. It is noted that the DSMC and USP-BGK methods use the same kind of computational particles and track particle motions in the same manner. The only difference between them is the implementation of the collision step. Therefore, the key and perhaps the only ingredient for accurate and efficient hybrid USPBGK-DSMC simulations is a proper equilibrium breakdown parameter. In the previous USPBGK-DSMC method for monatomic gases [29], a switching parameter P_s, which was determined by the local Knudsen number and the dimensionless time step, was introduced. In the present work, we directly employ this switching parameter, which is defined as

$$P_s = \begin{cases} 0 & \varepsilon / \Delta t \le 1.5 \\ 1 & \varepsilon / \Delta t > 1.5 \end{cases}. \tag{5.1}$$

This criterion involves the Knudsen number and also considers the balance of accuracy and efficiency. According to P_s, a USP-BGK or DSMC collision operator is called in the calculated cell. If $P_s = 0$, the USP-BGK collision process is performed; Otherwise, if $P_s = 1$, the hybrid scheme recovers DSMC, e.g., in the current work the Borgnakke-Larsen model for polyatomic gases [3] is employed. It is worth mentioning that, besides $\varepsilon / \Delta t$, other equilibrium-breakdown criteria, such as the gradient-length local (GLL) Knudsen number [46], are also possible in the present framework of the hybrid algorithm.

The detailed implementations of the proposed hybrid USPBGK-DSMC method for polyatomic gases are described in Fig. 1. Compared with the USP-BGK method in section 4, only an extra judgment needs to be added before the molecular collisions, i.e., estimating P_s in every computational cell after particle motion and determining the usage of DSMC or USP-BGK collision solver.

Although many hybrid methods based on DSMC combined with different equilibrium or near-equilibrium solvers already exist, e.g., continuum CFD-DSMC [34–36], equilibrium particle-DSMC [55], BGK-DSMC [28], Fokker-Planck-DSMC [30], the hybrid USPBGK-DSMC has some unique advantages. First, unlike the continuum CFD-DSMC method, USPBGK-DSMC is an "all-particle" method. Therefore, there is no need to transfer information between the continuum and particle regions, which causes accuracy and numerical instability issues well known in the hybrid continuum-particle method. Second, as the BGK model can be applied to a wider range of the Knudsen number than CFD solving the Navier-Stokes equations, the difficulty in positioning the hybrid interface can be much alleviated in USPBGK-DSMC, like other "all-particle" hybrid methods. Third, USP-BGK and DSMC store the same information in the computational particles and track their motions in the same manner. The only difference between the two methods is how to perform collision, which is a local process. Therefore, the combining of USP-BGK and DSMC requires a minimum amount of effort. Finally, as discussed earlier, USP-BGK has a higher order of accuracy. When combined with DSMC, the USPBGK-DSMC hybrid method can also achieve higher efficiency than the traditional BGK-DSMC hybrid one by using larger computational cell sizes and time steps.
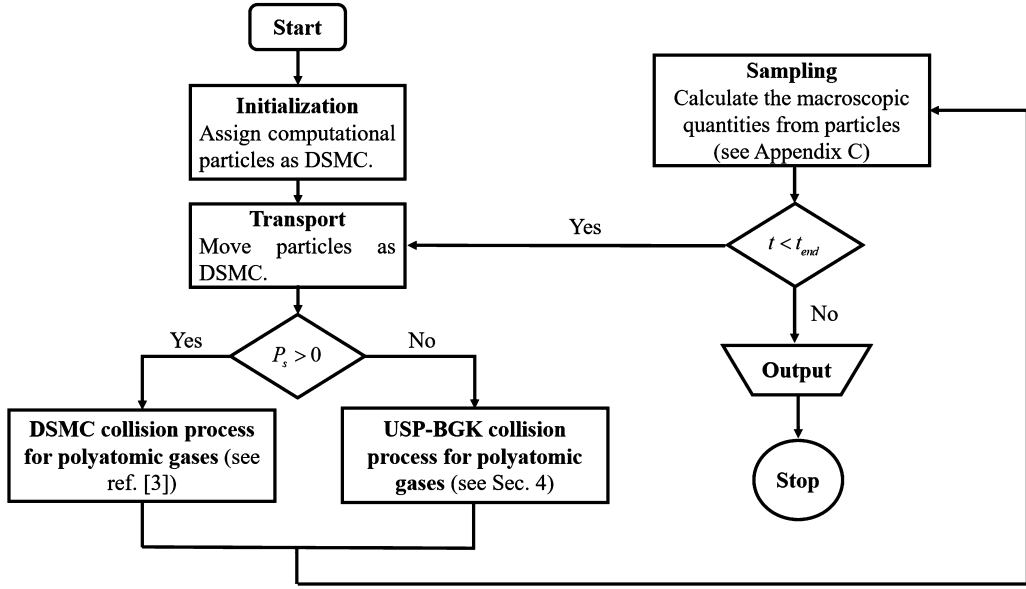
Fig. 1. Implementations of the hybrid USPBGK-DSMC method for polyatomic gases.

5.2. Determining the rotational and vibrational collision numbers in the hybrid scheme

In Dauvois et al.'s ES-BGK model [22] the rotational and vibrational energies relax to the intermediate translational-rotational temperature $T_{tr,rot}$ and equilibrium temperature T_{eq}, respectively. Using Eq. (A.1), their relaxation processes are described as

$$\frac{\partial E_{vib}}{\partial t} = -\frac{1}{Z_{vib}\tau_{BGK}} \left(E_{vib} - e_{vib}(T_{eq}) \right). \tag{5.2a}$$

$$\frac{\partial \left(E_{rot} - e_{rot}(T_{tr,rot}) \right)}{\partial t} = -\frac{1}{Z_{rot}\tau_{BGK}} \left(E_{rot} - e_{rot}(T_{tr,rot}) \right) \tag{5.2b}$$

In contrast, most continuum analyses use the Jeans equation to model rotational relaxation and the Landau-Teller equation to model vibrational relaxation [43]. To determine the rotational and vibrational collision numbers of the ES-BGK model, i.e., Z_{rot} and Z_{vib}, it is necessary to find their relationship with the continuum model, i.e., with Z_{rot}^{cont} and Z_{vib}^{cont}. For the continuum model, the relaxation of the rotational and vibrational energies can be written as

$$\frac{\partial E_{int}}{\partial t} = -\frac{1}{Z_{int}^{cont}\tau_c} (E_{int} - e_{int}(T_{tr})), \tag{5.3}$$

where τ_c is the mean collision time and the subscript "int" can be "rot" or "vib", indicating the rotational and vibrational relaxation processes, respectively. Comparing Eqs. (5.2a) and (5.3) yields

$$Z_{vib} = Z_{vib}^{cont} \frac{\tau_c}{\tau_{BGK}} \frac{e_{vib}(T_{vib}) - e_{vib}(T_{eq})}{e_{vib}(T_{vib}) - e_{vib}(T_{tr})}. \tag{5.4}$$

Similarly, comparing Eqs. (5.2b) and (5.3) yields

$$Z_{rot} = Z_{rot}^{cont} \frac{\tau_c}{\tau_{BGK}} \frac{e_{rot}(T_{rot}) - e_{rot}(T_{tr,rot}) + \frac{Z_{rot}}{Z_{vib}} \left(e_{rot}(T_{tr,rot}) - e_{rot}(T_{eq}) \right)}{e_{rot}(T_{rot}) - e_{rot}(T_{tr})}. \tag{5.5}$$

Assuming that rotational relaxation is much faster than vibrational relaxation, Eq. (5.5) can be further simplified as

$$Z_{rot} = Z_{rot}^{cont} \frac{\tau_c}{\tau_{BGK}} \frac{3}{3 + \delta_{rot}}. \tag{5.6}$$

It is noted that the relaxation of vibrational energy is different in the ES-BGK model than in the continuum model. In the ES-BGK model, the vibrational temperature relaxes to the equilibrium temperature, while it relaxes to the translational temperature in the continuum model. Therefore, in theory, the present ES-BGK model cannot recover the relaxation process of the continuum model when T_{vib} is quite close to T_{eq}, which might result in $Z_{vib} < Z_{rot}$. Correspondingly, the correction of Eq. (5.4) is also doubtful in such a limit. However, as $T_{vib} \to T_{eq}$, the flow field approaches equilibrium and the transfer

of the vibrational energy is negligible. Therefore, by adding the constraint $Z_{vib} \geq Z_{rot}$ to Eq. (5.4), we modify the correction of the vibrational collision number as

$$Z_{vib} = \max \left\{ Z_{vib}^{cont} \frac{\tau_c}{\tau_{BGK}} \frac{e_{vib}(T_{vib}) - e_{vib}(T_{eq})}{e_{vib}(T_{vib}) - e_{vib}(T_{tr})}, Z_{rot} \right\}. \tag{5.7}$$

In addition, to avoid the singularity at $T_{vib} = T_{tr}$, we also set $Z_{vib} = Z_{rot}$ at that point.

In addition, an improved ES-BGK model for polyatomic gases has been developed by Mathiaud et al. recently [56]. This model constructs the relaxation processes directly based on the Landau-Teller and Jeans relaxation equations. Therefore, from a physical point of view, it would be better than the Dauvois et al.'s ES-BGK model. From the aspect of the numerical scheme, the proposed USP-BGK method can be considered as a general methodology to develop high order stochastic particle method. The key point is the macro-micro decomposition of the collision term, as discussed in sec. 4.1. In principle, a continuous part of the collision term can be constructed as long as the BGK model is provided, and then a certain USP-BGK algorithm would be implemented as shown in section 4.2. Therefore, there is no technical difficulty in extending the current USP-BGK method for the improved ES-BGK model. The extension of the present method to other BGK models and the assessment of different models, including the one developed by Mathiaud et al., will be a future work.

For the DSMC method, the Borgnakke-Larsen model is employed in the present paper. It is known that the rotational and vibrational collision numbers are also different between DSMC and the continuum model. Therefore, similar to the situation in BGK, the modification of the internal collision numbers is also needed in DSMC. Here we directly use the results provided by Refs. [44,45], i.e.,

$$Z_{vib}^{DSMC} = Z_{vib}^{cont} \frac{\delta_T}{\delta_T + \delta_A} \quad \text{and} \quad Z_{rot}^{DSMC} = Z_{rot}^{cont} \frac{\delta_T}{\delta_T + \delta_{rot}}, \tag{5.8}$$

where $\delta_A = \delta_{vib}^2(T_{tr}) \exp(T_0/T_{tr})/2$ (see Ref. [44]) and $\delta_T = 4 - 2(\omega - 0.5)$ is the degrees of freedom of the relative translational energy. ω is the power-law exponent of the viscosity-temperature dependence, i.e.,

$$\mu = \mu_{ref} \left(T_{tr}/T_{ref} \right)^{\omega}, \tag{5.9}$$

where T_{ref} and μ_{ref} are the reference temperature and viscosity, respectively.

In particular, for nitrogen gas, which is considered for the numerical cases presented in the next section, the rotational collision number of the continuum model is obtained as [46]

$$Z_{rot}^{cont} = Z_{rot}^{\infty} \left/ \left[1 + \frac{\pi^{3/2}}{2} \left(\frac{T^*}{T_{tr}} \right)^{1/2} + \left(\frac{\pi^2}{4} + \pi \right) \left(\frac{T^*}{T_{tr}} \right) \right] \right., \tag{5.10}$$

where $Z_{rot}^{\infty} = 18.1$ and $T^* = 91.5$ K. The vibrational collision number is set to

$$Z_{vib}^{cont} = \frac{\tau_{MW} + \tau_p}{\tau_c}, \tag{5.11}$$

where Millikan-White correlated vibrational relaxation time τ_{MW} is written as

$$\tau_{MW} = \frac{1}{p} \exp \left[\left(A T_{tr}^{-1/3} - B \right) - 18.42 \right] \tag{5.12}$$

with $A = 221$ and $B = 12.3$ for nitrogen. With Park's high-temperature correction one obtains

$$\tau_p = \sqrt{\frac{\pi m}{8 k_B T_{tr}}} / (\sigma_s n), \tag{5.13}$$

where a reference collision cross-section of $\sigma_s = 5.81 \times 10^{-21}$ m^2 is used.

6. Numerical simulations

In this section, four typical 1D and 2D gas flows were simulated and analyzed. An exponentially weighted moving time-averaging technique [9] was employed for steady flows to reduce statistical noise. Thus, any macro variables Φ^{n+1} at the time step t^{n+1}, such as density, moments and energies, are calculated as

$$\Phi^{n+1} = \frac{n_a - 1}{n_a} \Phi^n + \frac{1}{n_a} \Phi(t), \tag{6.1}$$

where n_a is the number of time steps used for averaging and $\Phi(t)$ denotes the macro quantities sampled at the current time.

Table 1

Computational parameters for the relaxation in a homogeneous flow.

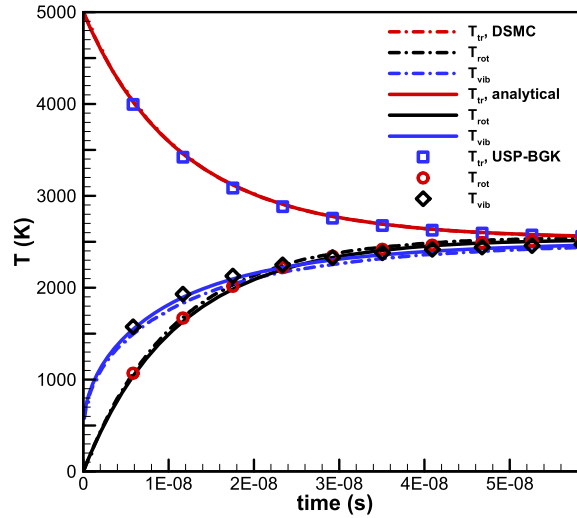| Density (kg/m^3)	Translational temperature (K)	Rotational temperature (K)	Vibrational temperature (K)
1.741×10^{-2}	5000	0	0

Fig. 2. Comparison of rotational and vibrational relaxation in a homogeneous flow. (For interpretation of the colors in the figure(s), the reader is referred to the web version of this article.)

6.1. Rotational and vibrational relaxation in a homogeneous flow

The proposed USP-BGK method for polyatomic gases first was tested for the relaxation problem in a homogeneous nitrogen flow. For DSMC the variable-hard-sphere (VHS) model was employed with a reference diameter of 4.17×10^{-10} m at $T_{ref} = 273$ K, and the reference viscosity is $\mu_{ref} = 1.6734 \times 10^{-5}$ Pa·s with a power-law exponent of $\omega = 0.75$. As shown in Table 1, the gas density is initially set as 1.741×10^{-2} kg/m^3. The initial translational temperature is 5000 K, and both initial rotational and vibrational temperatures are 0 K. The rotational and vibrational collision numbers are assumed to be constant, i.e., $Z_{rot}^{cont} = 5$ and $Z_{vib}^{cont} = 10$. According to the ES-BGK model, the analytical solutions of translational, rotational and vibrational temperature relaxations can be calculated from Eqs. (B.2) and (B.3). Fig. 2 compares the relaxations obtained by DSMC, USP-BGK and from the analytical solution of the ES-BGK model. The time step sizes of DSMC and USP-BGK are $0.2\tau_c$ and $10\tau_c$, respectively. According to the initial condition, the mean collision time τ_c is calculated as 5.844×10^{-10} s. As shown in Fig. 2, the USP-BGK method provides the correct relaxation rate of internal energies. Note that DSMC (dashed lines) and analytical solutions of the translational temperature (solid lines) lie on top of each other.

6.2. Shock structure

Shock wave is one of typical nonequilibrium flows. The structures of translational, rotational and vibrational temperatures usually do not overlap due to their distinguished relaxation rates. In the current case, where the nitrogen is considered, the pre-shock temperature, number density and Mach number are $T_1 = 226.149$ K, $n_1 = 3.745 \times 10^{23}$ m^{-3} and $Ma_1 = 15$, respectively. According to the shock relations, in the post-shock side $T_2 = 8295.14$ K, $n_2 = 2.793 \times 10^{24}$ m^{-3} and $Ma_2 = 0.344$. Note that the shock condition for two specific heat ratios can be found in Ref. [47]. The same DSMC model is employed as that in Sec. 6.1. The rotational and vibrational relaxation numbers are assumed to be constant, i.e., $Z_{rot}^{cont} = 5$ and $Z_{vib}^{cont} = 20$. The size of the computational domain is 100λ, where $\lambda = 4.734 \times 10^{-6}$ m is the mean free path length on the pre-shock side. For DSMC 100 uniform cells were employed, while for the USP-BGK and hybrid USPBGK-DSMC methods 50 uniform cells were used. The CFL criterion is based on the pre-shock condition resulting in $CFL = 0.5$ for all schemes. The computational parameters for the shock wave flow are also presented in Table 2.

Density, translational, rotational and vibrational temperature structures are shown in Fig. 3. It can be observed that the results of DSMC and USPBGK-DSMC agree well with each other. However, the USP-BGK results deviate from the DSMC data due to the failure of the BGK model ahead of the shock wave. The blue line in Fig. 3(a) refers to the switching parameter of Eq. (5.1), which indicates the separation of the computational domain.

Table 2
Computational parameters for the shock wave flow.

	Number density (m^{-3})	Temperature (K)	Mach number
Pre-shock	3.745×10^{23}	226.149	15.0
Post-shock	2.793×10^{24}	8295.14	0.344
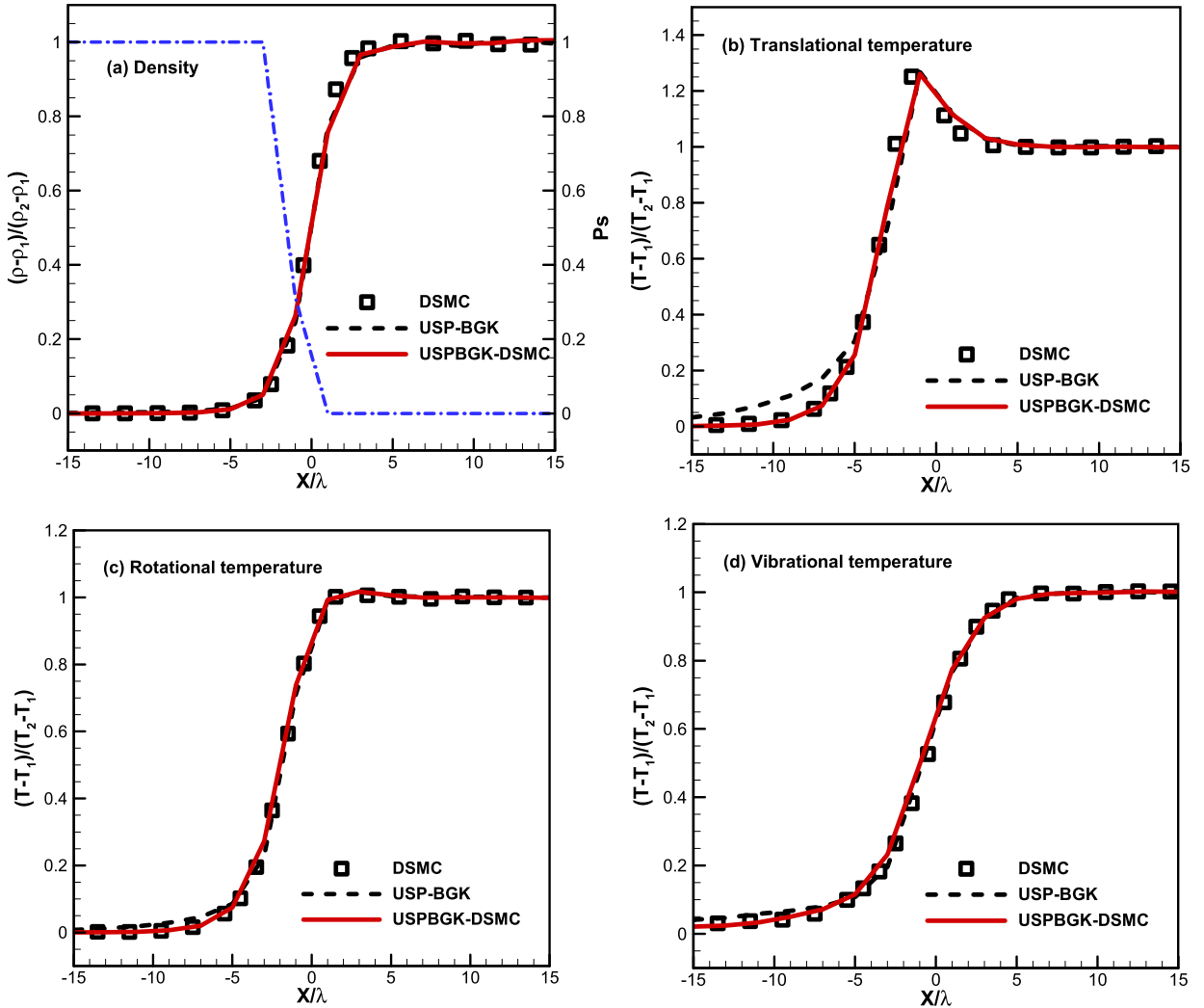
Fig. 3. Comparison of density, translational, rotational and vibrational temperatures across the shock wave. $\lambda = 4.734 \times 10^{-6}$ m is the mean free path length on the pre-shock side.

6.3. Hypersonic flow past a wedge

Hypersonic flow passing across a wedge with a sharp leading edge was calculated and presented. This flow is characterized by an attached shock and nonequilibrium regions near the leading edge, the boundary layer and the wake. The computational setup is the same as the Ref. [48]. The wedge half-angle is 10-deg and the computational domain is a rectangular box of 0.8×2.5 m^2; see the schematic in Fig. 4, which also depicts the unstructured meshes. The other computational parameters are given in Table 3. Nitrogen inflow with a number density of $n_\infty = 2.124 \times 10^{21}$ m^{-3} at a temperature of $T_\infty = 200$ K is considered, and the freestream velocity is $U_\infty = 2883$ m/s (Ma=10). The wedge wall temperature is 500 K and a fully diffusive wall condition is employed. The Knudsen number, calculated based on the freestream condition and the half-height of the wedge, is about 0.002. The bottom surface is treated as a symmetric boundary, while the other surfaces of the computational domain are inflow and outflow boundaries, respectively. About 27,000 cells were employed, and the particle number per cell was about 200 based on the freestream condition. The CFL number is set to 0.25. Rotational and
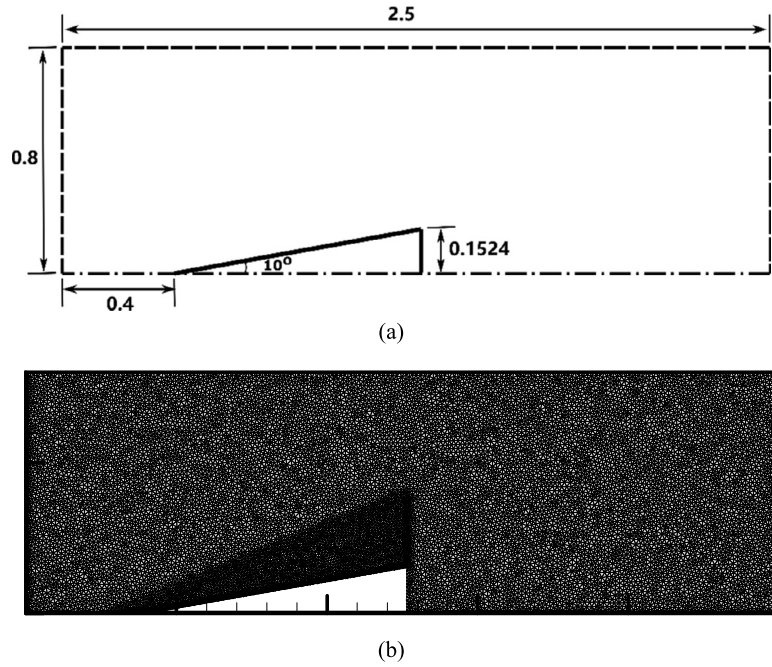
(a)

(b)

Fig. 4. Illustration of the wedge test case with (b) the computational grid.

Table 3
Computational parameters for the hypersonic flow past a wedge.

Inflow conditions			Wall boundary condition
Number density (m^{-3})	Temperature (K)	Velocity (m/s)	Temperature (K)
2.124×10^{21}	200	2883	500

vibrational collision numbers were set according to Eqs. (5.10)–(5.13). For DSMC the VHS model was used with a reference diameter of 4.11×10^{-10} m, and the reference temperature is $T_{ref} = 290$ K with a power-law exponent of $\omega = 0.7$.

Fig. 5(a) shows the distributions of Mach number and the separation regions of USP-BGK and DSMC for the calculation. It can be observed that the gas is very rarefied in the wake region so DSMC was employed there and the USP-BGK method was used in the rest of the domain. Fig. 5(b) presents the translational and rotational temperatures. Since the Knudsen number in the current case is small, translational and rotational relaxations are in equilibrium in most parts. However, minor differences can still be observed in the wake of the wedge due to the rarefaction effect. In addition, the vibrational energy in the present case is hardly excited due to low-temperature values.

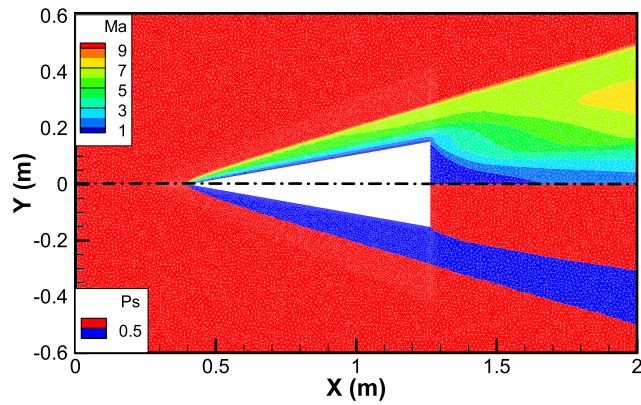Surface friction (C_F) and heating (C_H) coefficients are defined as

$$C_F = \sigma_{sur}/\left(\frac{1}{2}\rho_\infty U_\infty^2\right) \quad \text{and} \tag{6.2}$$

$$C_H = q_{sur}/\left(\frac{1}{2}\rho_\infty U_\infty^3\right), \tag{6.3}$$

where σ_{sur} and q_{sur} denote shear stress and heat flux on the surface, respectively. Further, ρ_∞ is the free-stream density and U_∞ is the free-stream velocity. The surface coefficients are plotted as functions of the distance S along the wedge surface normalized by the length L of the top surface. As shown in Fig. 6, the USPBGK-DSMC results are virtually identical to the DSMC reference data of [49].

6.4. Hypersonic flow past a cylinder

Hypersonic flow past a cylinder is another typical case to investigate multiscale gas flows. The computational setup is the same as the Ref. [46]. A nitrogen flow with a freestream number density of $n_\infty = 1.61 \times 10^{21}$ m^{-3} and initial temperatures of $T_{tr,\infty} = T_{rot,\infty} = T_{vib,\infty} = 217.5$ K is considered. The freestream velocity is 4510 m/s (Ma=15). The diameter of the cylinder is 0.08 m, and its surface temperature is 1000 K. A fully diffusive wall condition is employed. The computational parameters are also presented in Table 4. For DSMC the VHS model is used with a reference diameter of 4.17×10^{-10} m at
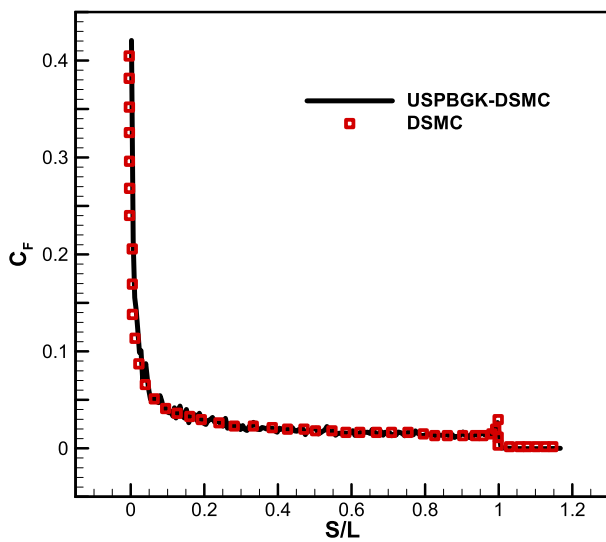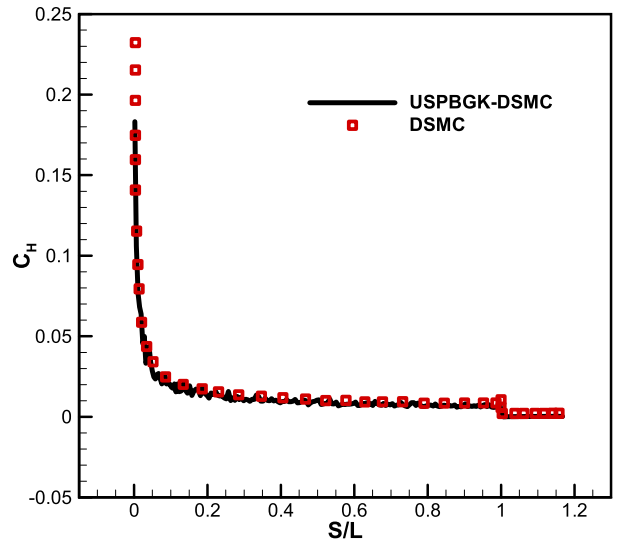
(a)
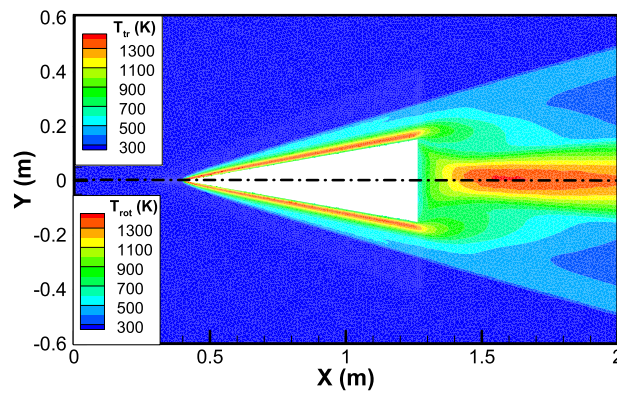
(b)

Fig. 5. Distribution of (a) Mach number and switching parameter; (b) the translational and rotational temperatures for a Mach 10 nitrogen flow past a wedge.

(a)

(b)

Fig. 6. (a) Surface friction and (b) heating coefficients for a Mach 10 nitrogen flow past a wedge. Solid line: USPBGK-DSMC; Square symbol: DSMC data given in Ref. [49].
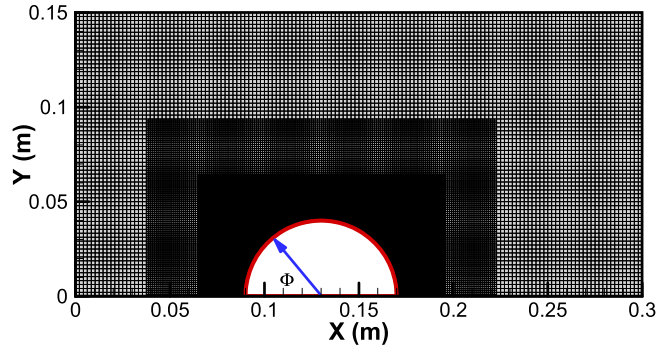
Fig. 7. Computational domain with successively refined grid for hypersonic flow past a cylinder.

Table 4

Computational parameters for the hypersonic flow past a cylinder.

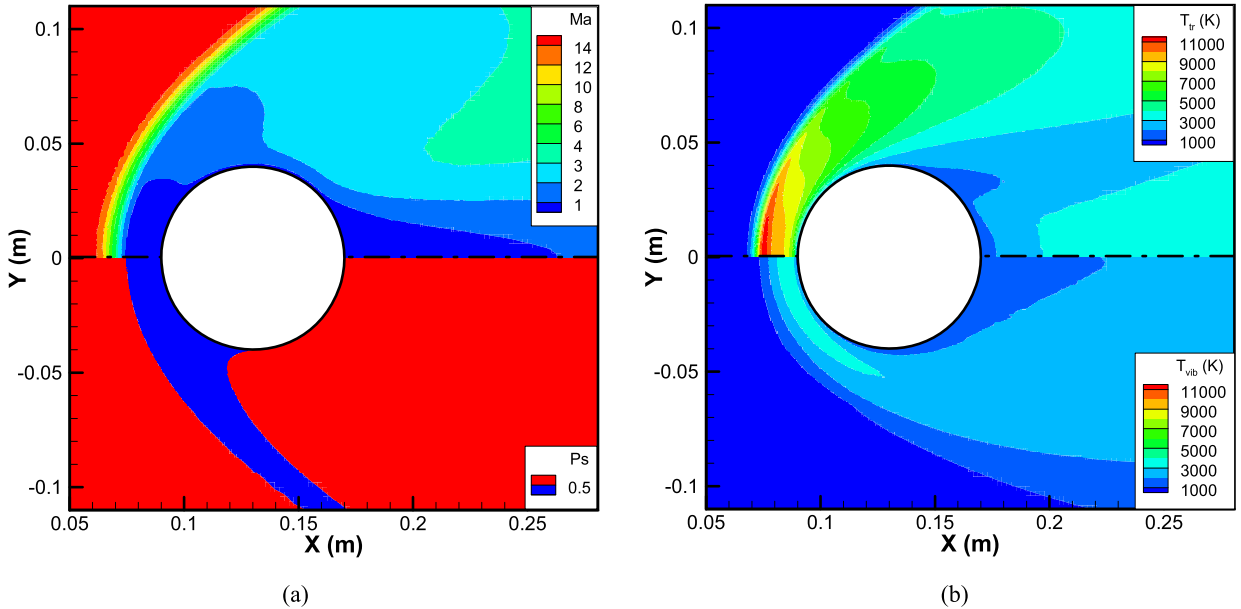| Inflow conditions			Wall boundary condition
Number density (m^{-3})	Temperature (K)	Velocity (m/s)	Temperature (K)
1.61×10^{21}	217.5	4510	1000

Fig. 8. Nitrogen flow around a cylinder at a Mach number of 15: Distribution of (a) Mach number and switching parameter; (b) translational and vibrational temperatures. The USPBGK-DSMC method was employed a coarse grid of 144×72.

$T_{ref} = 273$ K and a power-law exponent of $\omega = 0.75$. The rotational and vibrational collision numbers are set according to Eqs. (5.10)–(5.13). The Knudsen number equals 0.01 based on the free-stream condition and the cylinder diameter.

The computational domain is similar to the test case of argon gas flow past a cylinder in Ref. [29], i.e., a rectangular box of 0.3×0.15 m^2. As shown in Fig. 7, Cartesian grids with successive refinement were employed around the cylinder. For each refinement, the cell's width and height are half of those of the last coarser level. The bottom boundary is symmetrical, and the other boundaries are inlet/outlet flows. To investigate the accuracy of the proposed hybrid method, three types of cartesian grids were employed, i.e., 36×18, 72×36 and 144×72 grids for the coarsest level. About 36000 computational cells were employed for the case with 144×72 grids. In addition, for all simulations, the CFL number is set to be 0.5, and about 200 computational particles per coarse cell were initially assigned.

Fig. 8 shows the distributions of Mach number, translational and vibrational temperatures. The lower panel in Fig. 8(a) depicts the switching parameter P_s; one can observe the continuum regime in front of the cylinder where $P_s = 0$ and thus the USP-BGK method was employed. Fig. 9 presents translational, rotational and vibrational temperatures along an
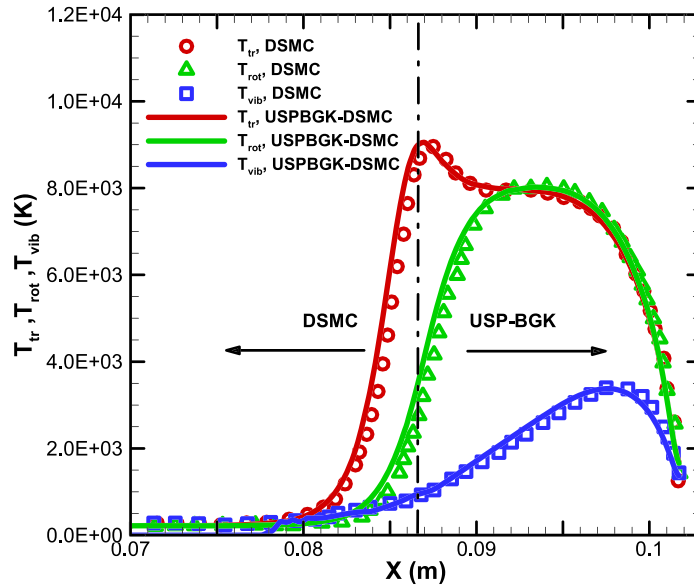
Fig. 9. Nitrogen flow around a cylinder at a Mach number of 15: Temperature distributions along the 45° extraction line. The black dash-dotted line refers to the interface between USP-BGK and DSMC. A coarse grid of 144×72 is employed in the USPBGK-DSMC method. Symbols: DSMC data of [46] and solid line: USPBGK-DSMC.
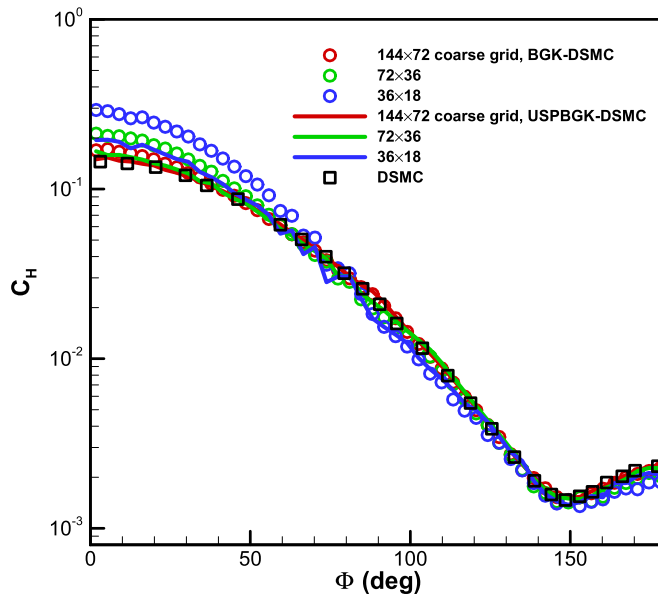

Fig. 10. Nitrogen flow around a cylinder at a Mach number of 15: Surface heating coefficient along the cylinder wall. Solid line: USPBGK-DSMC; Circle symbol: traditional BGK-DSMC; Square symbol: DSMC data of [46].

extraction line at an angle of 45°. It is clear that the hybrid USPBGK-DSMC method provides results consistent with the DSMC data in Ref. [46]. In addition, the black dash-dotted line indicates the interface between USP-BGK and DSMC regions.

The surface heating coefficient is calculated in Fig. 10. As cell size decreases, the USPBGK-DSMC method, which is second-order accurate in the continuum regime, approaches the reference data of DSMC faster than BGK-DSMC. Therefore, fewer grids are requested. In addition, the BGK-DSMC method used here is the same as USPBGK-DSMC, except for the stochastic particle BGK solver. The former employs the traditional SP-BGK method in Sec. 3, while the latter uses the proposed USP-BGK method in Sec. 4.

The L1-norm errors of the surface heating coefficient for the different grid sizes are given in Table 5. The calculations were run on the Euler cluster of ETH Zürich. The CPU time per time step also is presented. It can be seen that computational times of USPBGK-DSMC and BGK-DSMC are similar if the same cell sizes are employed. However, higher order of

Table 5
L_1-norm error of surface heating coefficient along the cylinder wall.

Number of coarse cells	BGK–DSMC			USPBGK–DSMC		
	L_1-norm error	Order	CPU time (s)	L_1-norm error	Order	CPU time(s)
36×18	0.5716	1.50	0.012	0.1291	2.64	0.016
72×36	0.2027	–	0.032	0.0207	–	0.042

convergence is obtained by the USPBGK-DSMC method. Therefore, the USPBGK-DSMC method can use larger time steps and fewer grids to achieve the same level of accuracy. As a result, the computational cost can be reduced significantly.

7. Conclusion

Employing the micro-macro decomposition of the ES-BGK collision term given in Ref. [22], the USP-BGK method was extended for applications of polyatomic gas flows. Since the algorithm of the USP-BGK method can be implemented in the same way as the traditional SP-BGK method and DSMC, we have shown that the construction of a hybrid scheme combining the USP-BGK method and DSMC is straightforward. The ES-BGK model and the related USP-BGK method for polyatomic gas have been validated by supersonic flows with strong shocks. Hypersonic flows past a wedge and a cylinder were also simulated by the hybrid USPBGK-DSMC method, and it has been demonstrated that the results agree well with the corresponding DSMC solutions. Note that for both test cases, a huge Knudsen number range from continuum to high rarefaction has to be modeled. Compared to the traditional stochastic particle methods, the efficiency of the proposed hybrid method is excellent and the computational cost is much lower. Therefore, the hybrid USPBGK-DSMC method is suitable for simulations of complex multiscale flows for polyatomic gases.

CRediT authorship contribution statement

Fei Fei: Conceptualization, Formal analysis, Methodology, Software, Validation, Writing – original draft. **Yuan Hu:** Formal analysis, Validation, Writing – review & editing. **Patrick Jenny:** Resources, Writing – review & editing.

Declaration of competing interest

The authors declare that they have no known competing financial interests or personal relationships that could have appeared to influence the work reported in this paper.

Data availability

Data will be made available on request.

Acknowledgements

Appendix A. Metropolis-Hastings (MH) algorithm

A Metropolis-Hastings method produces a Markov chain of samples from the target distribution [50] and has been employed to sample Chapman-Enskog [51] and ES-BGK distribution [52]. We also use the Metropolis-Hastings algorithm to generate the target distribution in the present work. The basic idea of the Metropolis-Hastings algorithm is to design a Markov chain with a transition probability $p(\mathbf{X}_{old}, \mathbf{X}_{new})$ between states, e.g. from $\mathbf{X}_{old}$ to $\mathbf{X}_{new}$. According to the reversibility condition, the transition probability should satisfy

$$f_t(\mathbf{X}_{old})p(\mathbf{X}_{old}, \mathbf{X}_{new}) = f_t(\mathbf{X}_{new})p(\mathbf{X}_{new}, \mathbf{X}_{old}), \tag{A.1}$$

where $f_t(\mathbf{X})$ is the target distribution and $\mathbf{X}$ is a stochastic variable. A simple way to satisfy this condition is to take [51]

$$p(\mathbf{X}_{old}, \mathbf{X}_{new}) = M(\mathbf{X}_{new}) \begin{cases} 1 & \text{if } f_t(\mathbf{X}_{new})M(\mathbf{X}_{old}) \geq f_t(\mathbf{X}_{old})M(\mathbf{X}_{new}) \\ \dfrac{f_t(\mathbf{X}_{new})M(\mathbf{X}_{old})}{f_t(\mathbf{X}_{old})M(\mathbf{X}_{new})} & \text{if } f_t(\mathbf{X}_{new})M(\mathbf{X}_{old}) < f_t(\mathbf{X}_{old})M(\mathbf{X}_{new}) \end{cases}, \tag{A.2}$$

where $M(\mathbf{X})$ can be chosen as a Maxwellian distribution, which is easily sampled. For example, to generate $f_t(\mathbf{X}) = \mathcal{F}_U$, we assume $M(\mathbf{X}) = \mathcal{F}_M$ as shown in Eq. (4.3), then the Metropolis-Hastings algorithm was implemented as follows:

(1) Draw $\mathbf{X}_{old} = \{\mathbf{V}_{old}, I_{r,old}, I_{v,old}\}$ from the Maxwellian distribution $\mathcal{F}_M$; select a new value if $\mathcal{F}_U(\mathbf{X}_{old}) < 0$.

(2) Draw a new value $\mathbf{X}_{new}$ from the Maxwellian distribution.

(3) Draw a random number *Rand* between 0 and 1; if $Rand \leq \min\left(1, \dfrac{\mathcal{F}_U(\mathbf{X}_{new})\mathcal{F}_M(\mathbf{X}_{old})}{\mathcal{F}_U(\mathbf{X}_{old})\mathcal{F}_M(\mathbf{X}_{new})}\right)$ then accept the "move" and set $\mathbf{X}_{old} = \mathbf{X}_{new}$; otherwise keep the current value of $\mathbf{X}_{old}$.

(4) Repeat steps 2 and 3 until N_{try} attempted moves have been made. Here, we set $N_{try} = 10 \sim 35$ as Ref. [52].

Similarly, this implementation can also be employed to generate other distributions in this paper.

Appendix B. Relaxation of the ES-BGK model

Note that the density $\rho(t)$, the mean velocity $\mathbf{U}(t)$ and the equilibrium temperature $T_{eq}(t)$ are constant during the collision step, while $\mathbf{\Pi}(t)$, $E_{tr}(t)$, $E_{rot}(t)$ and $E_{vib}(t)$ can be obtained by solving the moment equation of Eq. (3.1b).

Multiplying Eq. (3.1b) by $C^2/2$, I_r and iRT_0, and integrating over the phase space, we obtain

$$\frac{\partial}{\partial t}\begin{pmatrix} E_{tr}(t) \\ E_{rot}(t) \\ E_{vib}(t) \end{pmatrix} = \frac{\eta}{\tau_{BGK}}\begin{pmatrix} e_{tr}(T_{eq}) - E_{tr}(t) \\ e_{rot}(T_{eq}) - E_{rot}(t) \\ e_{vib}(T_{eq}) - E_{vib}(t) \end{pmatrix} + \frac{(1-\eta)}{\tau_{BGK}}\begin{pmatrix} -\frac{\delta_{rot}\theta}{3+\delta_{rot}} & \frac{3\theta}{3+\delta_{rot}} & 0 \\ \frac{\delta_{rot}\theta}{3+\delta_{rot}} & -\frac{3\theta}{3+\delta_{rot}} & 0 \\ 0 & 0 & 0 \end{pmatrix}\begin{pmatrix} E_{tr}(t) \\ E_{rot}(t) \\ E_{vib}(t) \end{pmatrix}. \tag{B.1}$$

Assuming $a_1 = E_{tr} + E_{rot}$ and $a_2 = (\delta_{rot}/3)E_{tr} - E_{rot}$, the solution of Eq. (B.1) is obtained as

$$a_1(t) = \exp\left(-\frac{\eta t}{\tau_{BGK}}\right)a_1(0) + \left[1 - \exp\left(-\frac{\eta t}{\tau_{BGK}}\right)\right]\left(e_{tr}(T_{eq}) + e_{rot}(T_{eq})\right), \tag{B.2a}$$

$$a_2(t) = \exp\left[-\frac{((1-\eta)\theta + \eta)t}{\tau_{BGK}}\right]a_2(0), \tag{B.2b}$$

$$E_{vib}(t) = \exp\left(-\frac{\eta t}{\tau_{BGK}}\right)E_{vib}(0) + \left[1 - \exp\left(-\frac{\eta t}{\tau_{BGK}}\right)\right]e_{vib}(T_{eq}). \tag{B.2c}$$

Therefore,

$$E_{tr}(t) = \frac{3}{3+\delta_{rot}}(a_1 + a_2) \quad \text{and} \quad E_{rot}(t) = \frac{\delta_{rot}a_1 - 3a_2}{3+\delta_{rot}}. \tag{B.3}$$

Besides $E_{tr}(t)$ and $E_{rot}(t)$, $\mathbf{\Pi}(t)$ is depended on the shear stress $\boldsymbol{\sigma} = \Theta - RT_{tr}\mathbf{I}$. Multiplying Eq. (3.1b) by $\mathbf{C} \otimes \mathbf{C} - C^2/3$ and integrating over the phase space, we have

$$\frac{\partial\boldsymbol{\sigma}(t)}{\partial t} = -\frac{1}{\tau_{BGK}}[1 - (1-\eta)(1-\theta)\nu]\boldsymbol{\sigma}(t). \tag{B.4}$$

Therefore,

$$\boldsymbol{\sigma}(t) = e^{-t/(\tau_{BGK}\,\text{Pr})}\boldsymbol{\sigma}(0). \tag{B.5}$$

According to Eq. (2.9), $\mathbf{\Pi}(t)$ reads

$$\mathbf{\Pi}(t) = \eta RT_{eq}\mathbf{I} + (1-\eta)\left[\theta RT_{tr,rot}(t)\mathbf{I} + (1-\theta)(\nu\boldsymbol{\sigma}(t) + RT_{tr}(t)\mathbf{I})\right], \tag{B.6}$$

Appendix C. Macro variables averaged from the auxiliary distribution

First considering the auxiliary distribution $\tilde{\mathcal{F}}^* = \mathcal{F}^* - \dfrac{\Delta t}{2}Q_C^*$, since the continuous part of the collision term also satisfies the conservation law, therefore, for the conserved variables, such as the density, mean velocity and total energy, we have

$$\rho = \left\langle\tilde{\mathcal{F}}^*\right\rangle_{V,I_r,I_v} = \left\langle\mathcal{F}^*\right\rangle_{V,I_r,I_v}, \qquad \rho\mathbf{U} = \left\langle\mathbf{V}\tilde{\mathcal{F}}^*\right\rangle_{V,I_r,I_v} = \left\langle\mathbf{V}\mathcal{F}^*\right\rangle_{V,I_r,I_v} \quad \text{and}$$

$$\rho E = \left\langle\left(\frac{1}{2}C^2 + I_r + I_v\right)\tilde{\mathcal{F}}^*\right\rangle_{V,I_r,I_v} = \left\langle\left(\frac{1}{2}C^2 + I_r + I_v\right)\mathcal{F}^*\right\rangle_{V,I_r,I_v}. \tag{C.1}$$

For the shear stress, multiplying Eq. (4.18a) by $\mathbf{C} \otimes \mathbf{C} - C^2/3$ and integrating over the phase space, we obtain

$$\boldsymbol{\sigma}^* = \tilde{\boldsymbol{\sigma}}^* \Big/ \left(1 + \frac{\Delta t}{2\varepsilon\,\text{Pr}}\right). \tag{C.2}$$

For the heat flux, multiplying Eq. (4.18a) by $\dfrac{1}{2}\mathbf{C}C^2$, $\mathbf{C}I_r$ and $\mathbf{C}I_v$, and integrating over the phase space, the heat flux related to the translational ($\mathbf{q}_{tr}^*$), rotational ($\mathbf{q}_{rot}^*$) and vibrational ($\mathbf{q}_{vib}^*$) energies yields

$$\mathbf{q}^*_{tr} = \tilde{\mathbf{q}}^*_{tr} \Big/ \left(1 + \frac{\Delta t}{2\varepsilon}\right), \qquad \mathbf{q}^*_{rot} = \tilde{\mathbf{q}}^*_{rot} \Big/ \left(1 + \frac{\Delta t}{2\varepsilon}\right) \quad \text{and} \quad \mathbf{q}^*_{vib} = \tilde{\mathbf{q}}^*_{vib} \Big/ \left(1 + \frac{\Delta t}{2\varepsilon}\right). \tag{C.3}$$

The total heat flux is $\mathbf{q}^*_{tr} + \mathbf{q}^*_{rot} + \mathbf{q}^*_{vib}$.

For the translational, rotational and vibrational energies, multiplying Eq. (4.18a) by $\phi = \left(\frac{1}{2}C^2, I_r, I_v\right)^T$ and integrating over the phase space again, we have

$$\tilde{E}^*_{tr} = E^*_{tr} - \frac{\Delta t}{2\varepsilon} \left[\eta \left(\frac{3}{2}T_{eq} - E^*_{tr}\right) + (1-\eta)\left(\frac{3\theta}{3+\delta_{rot}}E^*_{rot} - \frac{\theta\delta_{rot}}{3+\delta_{rot}}E^*_{tr}\right) \right], \tag{C.4}$$

$$\tilde{E}^*_{rot} = E^*_{rot} - \frac{\Delta t}{2\varepsilon} \left[\eta \left(\frac{\delta_{rot}}{2}T_{eq} - E^*_{rot}\right) + (1-\eta)\left(-\frac{3\theta}{3+\delta_{rot}}E^*_{rot} + \frac{\theta\delta_{rot}}{3+\delta_{rot}}E^*_{tr}\right) \right], \tag{C.5}$$

$$\tilde{E}^*_{vib} = E^*_{vib} - \frac{\Delta t}{2\varepsilon} \left[\eta \left(e_{vib}(T_{eq}) - E^*_{vib}\right) \right]. \tag{C.6}$$

After organizing, the translational, rotational and vibrational energies after the transport step yield

$$E^*_{tr} = \frac{\eta \frac{3\Delta t}{2\varepsilon}\frac{3+\delta_{rot}}{2}T_{eq} + 3\left(\tilde{E}^*_{tr} + \tilde{E}^*_{rot}\right)}{\left(1 + \frac{\Delta t}{2\varepsilon}\eta\right)(3+\delta_{rot})} + \frac{\left(\delta_{rot}\tilde{E}^*_{tr} - 3\tilde{E}^*_{rot}\right)}{\left(1 + \frac{\Delta t}{2\varepsilon}(\eta + (1-\eta)\theta)\right)(3+\delta_{rot})}, \tag{C.7}$$

$$E^*_{rot} = \frac{\eta \frac{\delta_{rot}\Delta t}{2\varepsilon}\frac{3+\delta_{rot}}{2}T_{eq} + \delta_{rot}\left(\tilde{E}^*_{tr} + \tilde{E}^*_{rot}\right)}{\left(1 + \frac{\Delta t}{2\varepsilon}\eta\right)(3+\delta_{rot})} - \frac{\left(\delta_{rot}\tilde{E}^*_{tr} - 3\tilde{E}^*_{rot}\right)}{\left(1 + \frac{\Delta t}{2\varepsilon}(\eta + (1-\eta)\theta)\right)(3+\delta_{rot})}, \tag{C.8}$$

$$E^*_{vib} = \frac{\tilde{E}^*_{vib} + \eta\frac{\Delta t}{2\varepsilon}e_{vib}(T_{eq})}{\left(1 + \eta\frac{\Delta t}{2\varepsilon}\right)}. \tag{C.9}$$

Similar results can be calculated from Eq. (4.18b), and the translational, rotational and vibrational energies after the collision step are averaged from the auxiliary distribution $\widehat{\mathcal{F}}$. In addition, since $\langle \phi Q_C(\mathcal{F}) \rangle_{V,I_r,I_v} = \langle \phi Q(\mathcal{F}) \rangle_{V,I_r,I_v}$ as shown in Eq. (4.6), E^*_{tr}, E^*_{rot} and E^*_{vib} keep constant during the collision step. Therefore, $\widehat{E}_{tr}$, $\widehat{E}_{vib}$ and $\widehat{E}_{vib}$ can also be calculated from the values before the collision step, i.e.,

$$\widehat{E}_{tr} = E^*_{tr} + \frac{\Delta t}{2\varepsilon} \left[\eta \left(\frac{3}{2}T_{eq} - E^*_{tr}\right) + (1-\eta)\left(\frac{3\theta}{3+\delta_{rot}}E^*_{rot} - \frac{\theta\delta_{rot}}{3+\delta_{rot}}E^*_{tr}\right) \right], \tag{C.10}$$

$$\widehat{E}_{vib} = E^*_{rot} + \frac{\Delta t}{2\varepsilon} \left[\eta \left(\frac{\delta_{rot}}{2}T_{eq} - E^*_{rot}\right) + (1-\eta)\left(-\frac{3\theta}{3+\delta_{rot}}E^*_{rot} + \frac{\theta\delta_{rot}}{3+\delta_{rot}}E^*_{tr}\right) \right], \tag{C.11}$$

$$\widehat{E}_{vib} = E^*_{vib} + \frac{\Delta t}{2\varepsilon} \left[\eta \left(e_{vib}(T_{eq}) - E^*_{vib}\right) \right]. \tag{C.12}$$

In the above, the hat "$\sim$" and "$\frown$" denote the variables averaged from $\tilde{\mathcal{F}}$ and $\widehat{\mathcal{F}}$, respectively.

References

[1] M.S. Ivanov, S.F. Gimelshein, Computational hypersonic rarefied flows, Annu. Rev. Fluid Mech. 30 (1998) 469–505.
[2] C. Park, Nonequilibrium Hypersonic Aerothermodynamics, John Wiley & Sons, 1990.
[3] G.A. Bird, Molecular Gas Dynamics and the Direct Simulation of Gas Flows, Clarendon, Oxford, 1994.
[4] L. Pareschi, G. Russo, Time relaxed Monte Carlo methods for the Boltzmann equation, SIAM J. Sci. Comput. 23 (2001) 1253–1273.
[5] S. Jin, Runge–Kutta methods for hyperbolic conservation laws with stiff relaxation terms, J. Comput. Phys. 122 (1995) 51–67.
[6] S.K. Stefanov, On DSMC calculation of rarefied gas flows with small number of particles in cells, SIAM J. Sci. Comput. 33 (2011) 677–702.
[7] W. Ren, H. Liu, S. Jin, An asymptotic-preserving Monte Carlo method for the Boltzmann equation, J. Comput. Phys. 276 (2014) 380–404.
[8] E.P. Gross, P.L. Bhatnagar, M. Krook, A model for collision processes in gases, Phys. Rev. 94 (3) (1954) 511–525.
[9] P. Jenny, M. Torrilhon, S. Heinz, A solution algorithm for the fluid dynamic equations based on a stochastic model for molecular motion, J. Comput. Phys. 229 (2010) 1077–1098.
[10] M.A. Gallis, J.R. Torczynski, The Application of the BGK Model in Particle Simulations, AIAA Paper 2000-2360, 2000.
[11] M.H. Gorji, P. Jenny, An efficient particle Fokker–Planck algorithm for rarefied gas flows, J. Comput. Phys. 263 (2014) 325–343.
[12] C. Baranger, Y. Dauvois, G. Marois, J. Mathé, J. Mathiaud, L. Mieussens, A BGK model for high temperature rarefied gas flows, Eur. J. Mech. B, Fluids 80 (2020) 1–12.
[13] B. Rahimi, H. Struchtrup, Capturing non-equilibrium phenomena in rarefied polyatomic gases: a high-order macroscopic model, Phys. Fluids 26 (5) (2014) 052001.
[14] Z. Wang, H. Yan, Q. Li, K. Xu, Unified gas-kinetic scheme for diatomic molecular flow with translational, rotational, and vibrational modes, J. Comput. Phys. 350 (2017) 237–259.
[15] T. Arima, T. Ruggeri, M. Sugiyama, Rational extended thermodynamics of a rarefied polyatomic gas with molecular relaxation processes, Phys. Rev. E 96 (2017) 042143.
[16] S. Kosuge, H.-W. Kuo, K. Aoki, A kinetic model for a polyatomic gas with temperature-dependent specific heats and its application to shock-wave structure, J. Stat. Phys. 177 (2) (2019) 209–251.

[17] J.L. Wu, Z.H. Li, Z.B. Zhang, A.P. Peng, On derivation and verification of a kinetic model for quantum vibrational energy of polyatomic gases in the gas-kinetic unified algorithm, J. Comput. Phys. 435 (2021) 109938.

[18] Lowell H. Holway Jr., New statistical models for kinetic theory: methods of construction, Phys. Fluids 9 (9) (1966) 1658–1673.

[19] E.M. Shakhov, Generalization of the Krook relaxation kinetic equation, Izv. Akad. Nauk SSSR, Meh. Židk. Gaza (1968) 142–145.

[20] V.A. Rykov, A model kinetic equation for a gas with rotational degrees of freedom, Fluid Dyn. 10 (6) (1975) 959–966.

[21] P. Andries, J.-P. Le Tallec, J.-P. Perlat, B. Perthame, The Gaussian-BGK model of Boltzmann equation with small Prandtl number, Eur. J. Mech. B, Fluids (2000) 813–830.

[22] Y. Dauvois, J. Mathiaud, L. Mieussens, An ES-BGK model for polyatomic gases in rotational and vibrational nonequilibrium, Eur. J. Mech. B, Fluids 88 (2021) 1–16.

[23] M.H. Gorji, P. Jenny, A Fokker–Planck based kinetic model for diatomic rarefied gas flows, Phys. Fluids 25 (6) (2013) 062002.

[24] J. Mathiaud, L. Mieussens, A Fokker–Planck model of the Boltzmann equation with correct Prandtl number for polyatomic gases, J. Stat. Phys. 168 (5) (2017) 1031–1055.

[25] J. Mathiaud, L. Mieussens, BGK and Fokker–Planck models of the Boltzmann equation for gases with discrete levels of vibrational energy, J. Stat. Phys. 178 (5) (2020) 1076–1095.

[26] F. Fei, J. Zhang, J. Li, Z.H. Liu, A unified stochastic particle Bhatnagar-Gross-Krook method for multiscale gas flows, J. Comput. Phys. 400 (2020) 108972.

[27] F. Fei, H.H. Liu, Z.H. Liu, J. Zhang, A benchmark study of kinetic models for shock waves, AIAA J. 58 (6) (2020) 2596–2608.

[28] R. Kumar, E. Titov, D.A. Levin, Development of a particle–particle hybrid scheme to simulate multiscale transitional flows, AIAA J. 51 (1) (2012) 200–217.

[29] F. Fei, P. Jenny, A hybrid particle approach based on the unified stochastic particle Bhatnagar-Gross-Krook and DSMC methods, J. Comput. Phys. 424 (2021) 109858.

[30] M.H. Gorji, P. Jenny, Fokker–Planck–DSMC algorithm for simulations of rarefied gas flows, J. Comput. Phys. 287 (2015) 110–129.

[31] S. Küchlin, P. Jenny, Parallel Fokker–Planck-DSMC algorithm for rarefied gas flow simulation in complex domains at all Knudsen numbers, J. Comput. Phys. 328 (2017) 258–277.

[32] S. Küchlin, P. Jenny, Automatic mesh refinement and parallel load balancing for Fokker–Planck-DSMC algorithm, J. Comput. Phys. 363 (2018) 140–157.

[33] E. Jun, M.H. Gorji, M. Grabe, et al., Assessment of the cubic Fokker-Planck-DSMC hybrid method for hypersonic rarefied flows past a cylinder, Comput. Fluids 168 (2018) 1–13.

[34] D.B. Hash, H.A. Hassan, Assessment of schemes for coupling Monte Carlo and Navier-Stokes solution methods, J. Thermophys. Heat Transf. 10 (1996) 242–249.

[35] Q. Sun, I.D. Boyd, G.V. Candler, A hybrid continuum/particle approach for modeling rarefied gas flows, J. Comput. Phys. 194 (2004) 256–277.

[36] T.E. Schwartzentruber, L.C. Scalabrin, I.D. Boyd, A modular particle–continuum numerical method for hypersonic non-equilibrium gas flows, J. Comput. Phys. 225 (2007) 1159–1174.

[37] H. Wijesinghe, N. Hadjiconstantinou, Discussion of hybrid atomistic-continuum methods for multiscale hydrodynamics, Int. J. Multiscale Comput. Eng. 2 (2004) 189–202.

[38] J.M. Burt, I.D. Boyd, Evaluation of a Particle Method for the Ellipsoidal Statistical Bhatnagar–Gross–Krook Equation, 44th AIAA Aerospace Science Meeting and Exhibit, AIAA Paper 2006-989, Reno, NV, Jan. 2006.

[39] O. Tumuklu, Z. Li, D.A. Levin, Particle ellipsoidal statistical Bhatnagar–Gross–Krook approach for simulation of hypersonic shocks, AIAA J. 54 (12) (2016) 3701–3716.

[40] M. Pfeiffer, Extending the particle ellipsoidal statistical Bhatnagar-Gross-Krook method to diatomic molecules including quantized vibrational energies, Phys. Fluids 30 (2018) 116103.

[41] F. Fei, Y. Ma, J. Wu, J. Zhang, An efficient algorithm of the unified stochastic particle Bhatnagar-Gross-Krook method for the simulation of multi-scale gas flows, Adv. Aerodyn. 3 (2021) 18.

[42] C. Ollivier-Gooch, M. Van Altena, A high-order-accurate unstructured mesh finite-volume scheme for the advection–diffusion equation, J. Comput. Phys. 181 (2) (2002) 729–752.

[43] B.L. Hass, D.B. Hash, G.A. Bird, F.E. Lumpkin, H.A. Hassan, Rates of thermal relaxation in direct simulation Monte Carlo methods, Phys. Fluids 6 (6) (1994) 2191–2201.

[44] N.E. Gimelshein, S.F. Gimelshein, D.A. Levin, Vibrational relaxation rates in the direct simulation Monte Carlo method, Phys. Fluids 14 (2002) 4452–4455.

[45] F.E. Lumpkin, B.L. Haas, I.D. Boyd, Resolution of differences between collision number definitions in particle and continuum simulations, Phys. Fluids A 3 (9) (1991) 2282–2284.

[46] T.R. Deschenes, I.D. Boyd, Extension of a modular particle-continuum method to vibrationally excited hypersonic flows, AIAA J. 49 (9) (2011) 1951–1959.

[47] J.J. Liu, Two-gamma jump relations for gaseous detonation waves, Combust. Sci. Technol. 136 (1998) 199–220.

[48] A.J. Lofthouse, I.D. Boyd, Nonequilibrium aerothermodynamics of sharp-leading edges, in: 47th AIAA Aerospace Sciences Meeting Including the New Horizons Forum and Aerospace Exposition, 2009.

[49] A.J. Lofthouse, Nonequilibrium Hypersonic Aerothermodynamics Using the Direct Simulation Monte Carlo and Navier–Stokes Models, PhD Thesis, University of Michigan, 2008.

[50] S. Chib, E. Greenberg, Understanding the Metropolis-Hastings algorithm, Am. Stat. 49 (1995) 327–335.

[51] A.L. Garcia, B.J. Alder, Generation of the Chapman-Enskog distribution, J. Comput. Phys. 140 (1998) 66–70.

[52] M. Pfeiffer, Particle-based fluid dynamics: comparison of different Bhatnagar-Gross-Krook models and the direct simulation Monte Carlo method for hypersonic flows, Phys. Fluids 30 (10) (2018) 106106.

[53] F. Fei, P. Jenny, A high-order unified stochastic particle method based on the Bhatnagar-Gross-Krook model for multi-scale gas flows, Comput. Phys. Commun. 274 (2022) 108303.

[54] H. Struchtrup, Macroscopic Transport Equations for Rarefied Gas Flows: Approximation Method in Kinetic Theory, Springer, Berlin, Heidelberg, 2005.

[55] J.M. Burt, I.D. Boyd, A hybrid particle approach for continuum and rarefied flow simulation, J. Comput. Phys. 228 (2) (2009) 460–475.

[56] J. Mathiaud, L. Mieussens, M. Pfeiffer, An ES-BGK model for diatomic gases with correct relaxation rates for internal energies, preprint, https://doi.org/10.13140/RG.2.2.33131.00807, 2022.